



HAL
open science

Hydromechanical modelling of salt caverns subjected to cyclic hydrogen injection and withdrawal

Ever-Dennys Coarita-Tintaya, Fabrice Golfier, Dragan Grgic, Mountaka Souley, Long Cheng

► **To cite this version:**

Ever-Dennys Coarita-Tintaya, Fabrice Golfier, Dragan Grgic, Mountaka Souley, Long Cheng. Hydromechanical modelling of salt caverns subjected to cyclic hydrogen injection and withdrawal. Computers and Geotechnics, 2023, 162, pp.105690. 10.1016/j.compgeo.2023.105690 . hal-04274287

HAL Id: hal-04274287

<https://hal.science/hal-04274287>

Submitted on 16 Nov 2023

HAL is a multi-disciplinary open access archive for the deposit and dissemination of scientific research documents, whether they are published or not. The documents may come from teaching and research institutions in France or abroad, or from public or private research centers.

L'archive ouverte pluridisciplinaire **HAL**, est destinée au dépôt et à la diffusion de documents scientifiques de niveau recherche, publiés ou non, émanant des établissements d'enseignement et de recherche français ou étrangers, des laboratoires publics ou privés.

Hydromechanical modelling of salt caverns subjected to cyclic hydrogen injection and withdrawal

Ever-Dennys, Coarita-Tintaya^a, Fabrice Golfier^a, Dragan Grgic^a, Mountaka Souley^b and Long Cheng^a

The affiliations of the authors:

^a University of Lorraine (UL), CNRS, GeoRessources Laboratory, Nancy, France

^b National Institute for Industrial Environment and Risks (Ineris), Nancy, France

E-mail address of the corresponding author: ever-dennys.coarita-tintaya@univ-lorraine.fr

Abstract

The present work is devoted to the study of underground hydrogen storage in salt caverns. Based on the hydromechanical characteristics of rock salts obtained from some laboratory experiments, we propose a novel model that includes short- and long-term mechanical behaviour. Specifically, the short-term part incorporates the elastoplastic and instantaneous damage mechanisms. Concerning the long-term behaviour, in addition to the primary and secondary creep phases, the tertiary phase takes into account a delayed damage mechanism. As application, we performed a hydromechanical modelling of two vertical salt caverns with different depths based on existing hydrogen gas caverns, which are subjected to cyclic hydrogen injection and withdrawal (seasonal and daily scenarios). Gas transport is also modelled taking into account diffusion and advection mechanisms. Mechanical results indicate that the stability problem of a very deep cavern is more worrying in comparison with a shallow cavern, as expected. However, the gas extension is the same for both caverns because the gas flow is mainly by diffusion transport, while the permeability almost doesn't increase. Since field data at very depths are limited, a sensibility analysis of material properties was carried out to provide insight into key mechanisms that may occur. Typically, a decrease in mechanical properties increases the damage extent around deep cavern but did not lead to significant increase in the gas leakage extent. Under the assumptions made, these findings suggest that the use of salt caverns for green hydrogen storage, even with aggressive operating conditions to regulate variations between renewable energy production and peak power demands, should not significantly affect the stability of salt cavern nor promote an increase in hydrogen loss.

Keywords: rock salt, elastoplasticity, creep, damage, hydrogen storage, gas transport

List of symbols

We used the convention of negative compressions for stresses and strains

a_d	Parameter of the maximal instantaneous damage
a_p	Parameter of the dilatancy coefficient
A_k	Permeability model parameter
A_N	Viscosity at reference temperature in Norton's law
A_T	Dimensionless exponent of tertiary damage rate increase
b	Biot coefficient
b_d	Growth rate of the instantaneous damage
c	Cohesion of rock salt
c_{H_2}	Hydrogen concentration
\mathbb{C}^e	Fourth-order drained elasticity stiffness tensor
$\tilde{\mathbb{C}}^e$	Fourth-order drained elasto-damaged stiffness tensor
d_i	Instantaneous damage
d_{max}	Maximal instantaneous damage reached at peak strength
d_{max0}	Maximal instantaneous damage reached under uniaxial compression
d_t	Tertiary damage
D^*	Diffusion coefficient of hydrogen in water
E	Young's modulus
\vec{f}	Volume force vector
G_k	Shear modulus in Kelvin's model
$J_2 = \frac{1}{2} \mathbf{s} : \mathbf{s}$	Second invariant of the deviatoric stress tensor \mathbf{s}
$J_3 = \det \mathbf{s}$	Third invariant of the deviatoric stress tensor \mathbf{s}
k	Permeability
k_0	Intrinsic permeability of the intact material
k_1, k_2	Kelvin's model parameters
K_d	Drained compressibility modulus of the porous medium
K_f	Fluid compression modulus
M	Biot modulus
n	Porosity
n_N	Dimensionless exponent of Norton law
n_T	Dimensionless exponent of tertiary damage rate increase
p	Means stress
p_f	Pore pressure
p_b	Brine pressure

p_s	Geostatic pressure
p_g^{max}	Maximum gas pressure
p_g^{min}	Minimum gas pressure
q	Equivalent (von Mises) deviatoric stress
q^*	Undamaged equivalent deviatoric stress
\vec{q}	Fluid volumetric flux vector
\mathbf{s}	Deviatoric stress tensor
t	Time
Y_d	Thermodynamic force conjugated to the instantaneous damage
Y_0	Initial state of Y_d
α^p	Parameter of plastic hardening function
$\beta = \frac{d\varepsilon_v^p}{d\gamma_p}$	Dilatancy coefficient
β_0	Dilatancy coefficient for initial volumetric contraction
β_m	Dilatancy coefficient for volumetric dilatancy at large deformation
β_{m0}	Maximum dilatancy coefficient under uniaxial compressive conditions
β_{ult}	Dilatancy coefficient for maximum volumetric dilatancy
$\dot{\gamma}_p = \sqrt{\frac{3}{2} \dot{\boldsymbol{\varepsilon}}^p : \dot{\boldsymbol{\varepsilon}}^p}$	Plastic distortion rate
γ_p^*	Plastic distortion threshold for instantaneous damage initiation
γ_{ult}	Ultimate plastic distortion
\mathbf{I}	Second order identity tensor.
$\boldsymbol{\varepsilon}$	Total strain tensor
$\boldsymbol{\varepsilon}^e$	Elastic strain tensor
$\dot{\boldsymbol{\varepsilon}}^p$	Plastic strain tensor rate
$\dot{\boldsymbol{\varepsilon}}^p = \dot{\boldsymbol{\varepsilon}}^p - \frac{\text{tr } \dot{\boldsymbol{\varepsilon}}^p}{3} \mathbf{I}$	Deviatoric plastic strain rate
$\varepsilon_v = \text{tr } \boldsymbol{\varepsilon}$	Volumetric strain
ε_v^p	Volumetric plastic strain
ε_{tr}	Equivalent transient strain
$\dot{\boldsymbol{\varepsilon}}^c$	Creep strain rate
η_k	Viscosity in Kelvin's model
η_o^p	Elastic limit (a fraction of the peak strength)
θ	Lode angle
μ_f	Dynamic viscosity of the fluid
ν	Poisson's ratio
ρ_f	Fluid density

ρ_b	Brine density
ρ_s	Rock density
σ	Stress tensor
σ_{ref}	Reference equivalent deviatoric stress
$\sigma_1, \sigma_2, \sigma_3$	Principal stresses
ϕ	Friction angle of the rock salt
$\vec{\nabla}$	Nabla operator
$\langle x \rangle = 1/2 (x + x)$	Maccauley bracket

1. Introduction

The ambitious goal of building a decarbonized and competitive economy through the development of renewable energies will require successfully managing their electricity production. One solution consists in converting this electricity into hydrogen by electrolysis of water, then storing the gas thus produced. This promotes the development of massive hydrogen storage solutions to meet energy demand and mitigate the intermittency of wind and solar energy. Therefore, there is a consensus for large-scale underground hydrogen storage (Ozarslan 2012; Zivar et al. 2021), for instance in aquifers, depleted gas fields, and rock salt caverns. Storage in salt caverns, in particular, appears today to be one of the most interesting solutions, guaranteeing long-term stability and sealing integrity, due to the very low permeability and porosity, the good mechanical properties, as well as the self-healing characteristics of rock salt (Cosenza and Ghoreychi 1999). Methane but also hydrogen (but to address demands from oil refineries and not for energy market) was successfully stored for more than 30 years in salt caverns in the UK and USA. Even though these caverns have been operated for decades without notable incident, the experience gained with natural gas, commonly used to provide a seasonal supply can be very different from the future use of salt caverns for hydrogen storage. The importance of regulating variations between renewable energy production and peak power demands should, indeed, promote more frequent cycles of gas injection and withdrawal, perhaps even on a daily basis. These extreme operating conditions, leading to higher stresses in salt caverns, could affect cavern stability and induce the initiation and development of fractures. This, in turn, may modify the transport properties and thus potentially cause hydrogen leakage problems around the cavern. Consequently, the safety and feasibility aspect of using salt caverns for this clean and sustainable energy vector is still to be demonstrated.

In-situ characterisation and experimentation in salt caverns remain complex due to their difficult accessibility. Some geophysical techniques, such as sonar surveys, can be used to

determine the shape of the cavern and volume changes due to the effect of creep closure. Borehole tests are also carried out to determine brine leakage, rock mass permeability, borehole closure rate, as well as to assess in-situ stresses (Bérest et al. 2006). Temperature profile measurements in boreholes have also been reported in salt caverns during gas injection and withdrawal (Bérest 2019). This lack of in-situ data, however, emphasises the importance of the development of numerical forecasting modelling for a better assessment of operating conditions and safety issues.

Various theoretical and numerical analyses have thus been conducted in the past to investigate the different life cycle phases of underground salt cavern facilities from short- to long-term responses, including salt cavern construction, operation, and even abandonment (Heusermann et al. 2003). Caverns geometry and initial conditions have also been extensively investigated, considering the influence of salt cavern shape, salt cavern buried depth, initial anisotropic stresses and even non-soluble interbedded layers in the salt formation (Wang et al. 2011, 2013; Shahmorad et al. 2016). Multiphysics coupling for salt cavern gas storage has also been considered. Thermomechanical simulations have been performed to study gas cycling conditions (Brouard et al. 2012; Li et al. 2020), the influence of cavern shape and buried depth (Habibi et al. 2021), and even cavern blowout (Djizanne et al. 2014). In contrast, a full THM (Thermo-hydro-mechanical) modelling of salt caverns is still scarce and very few studies are available, such as those by Asgari et al. (2020) and Fang et al. (2022). But these large-scale simulations are generally conducted at the expense of a simplified description of hydromechanical features of rock salt.

The complex coupled hydromechanical behaviour of rock salt has been widely studied for many years. The most probably important developments may be those accounting for the mechanical behaviour of rock salt being driven by plastic deformation processes with a capacity for strain hardening and large creep ability (Senseny et al. 1992; Alkan et al. 2007; Fuenkajorn and Phueakphum 2010). At low effective confining pressure, dilatancy and extensional fractures can occur in deforming salt, producing significant permeability increase by many orders of magnitude (Peach and Spiers 1996; Schulze et al. 2001; Grgic et al. 2022). These characterisations have led to the development of various models for rock salt behaviour. Short- and long-terms behaviour models (Munson and Dawson 1979; Cristescu 1993; Aubertin et al. 1999; Heusermann et al. 2003; Khaledi et al. 2016), dilatancy models (Stormont et al. 1992; DeVries et al. 2005; Alkan et al. 2007), time-dependent damage and healing models (Hou 2003; Wu et al. 2019), unified and thermomechanical models (Zhou et al. 2011; Grgic 2016) have thus been derived. In this work, the proposed model distinguishes itself from well-known rock salt models such as the Multimechanism Deformation constitutive model (Munson

and Dawson 1979; Reedlunn et al. 2022) and the Lubby2 constitutive model (Heusermann et al. 2003), by incorporating the short-term behaviour of rock salt through an elastoplastic and damage model. For the long-term creep, our model follows a similar approach to that of Hou (2003), which upgraded the Lubby2 model by integrating tertiary damage. Therefore, this novel model allows for a more comprehensive understanding of the mechanical response of rock salt by considering damage mechanisms in both the short-term and long-term aspects of hydromechanical behaviour. Finally, this numerical model is applied to analyse the operation of hydrogen gas storage in salt caverns.

Due to the scarce information on the hydromechanical behaviour around salt caverns, in the present work we aim to contribute to the understanding of this behaviour for underground salt caverns subjected to hydrogen pressure cycling, especially in the case of intensive one. In this light, a short- and long-term constitutive model based on some key mechanisms of the mechanical behaviour of rock salt is firstly proposed. This model is implemented in the industrial code COMSOL Multiphysics® and verified and compared with experimental data. Then, the model is applied to study the rock mass response around the cavern under different conditions. A series of hydromechanical simulations for two vertical cavern configurations (shallow and deep) are performed and analysed for two cycling scenarios (seasonal and daily). Finally, results are discussed in terms of long-term stability of these caverns and hydrogen leakage extension.

2. Constitutive model for rock salt

2.1. Main assumptions

The proposed constitutive model is based on the state-of-the art knowledge on rock salt hydromechanical behaviour and some available experimental results (Senseny et al. 1992; Liang et al. 2007; Liu et al. 2020). A particular attention will be given to the features of a rock salt specimen (salt bed of the Alsace potash mines in eastern France) studied both by Thorel (1994) and Grgic et al. (2022) (Figure 1). The main assumptions are:

- Homogeneous and fully-saturated porous medium (only dissolved gas is present in the salt formation).
- Isotropic rock. Grgic et al. (2022) showed that the deformations in the studied rock are almost the same in the three main directions under hydrostatic compression test.
- From the stress-strain curves (Figure 1a – down and Figure 1b), for relatively low confining pressures (i.e., 5-10 MPa which corresponds to approximately 200-400 m depth) a significant part of the irreversible deformation is in the pre-peak phase (with respect to the total measured deformation). At higher confining pressures (i.e., at greater depths), the behaviour of the rock salt would be governed by the hardening

phase. Moreover, since the minimum hydrogen pressure is higher than [20%; 30%] of the overburden pressure, the confining pressure on the cavern wall is higher than 1 MPa. For this confining pressure the hardening phase is also relatively significant. Therefore, in the following, we will only limit ourselves to this phase. Regarding the volumetric strain, the rock salt shows dilatancy (Figure 1a - up), except for high confining pressures (higher than 10 MPa). In this work, the short-term behaviour is based on the elastoplastic and damage theories. This behaviour is characterised by a significant strain hardening phase and material dilatancy.

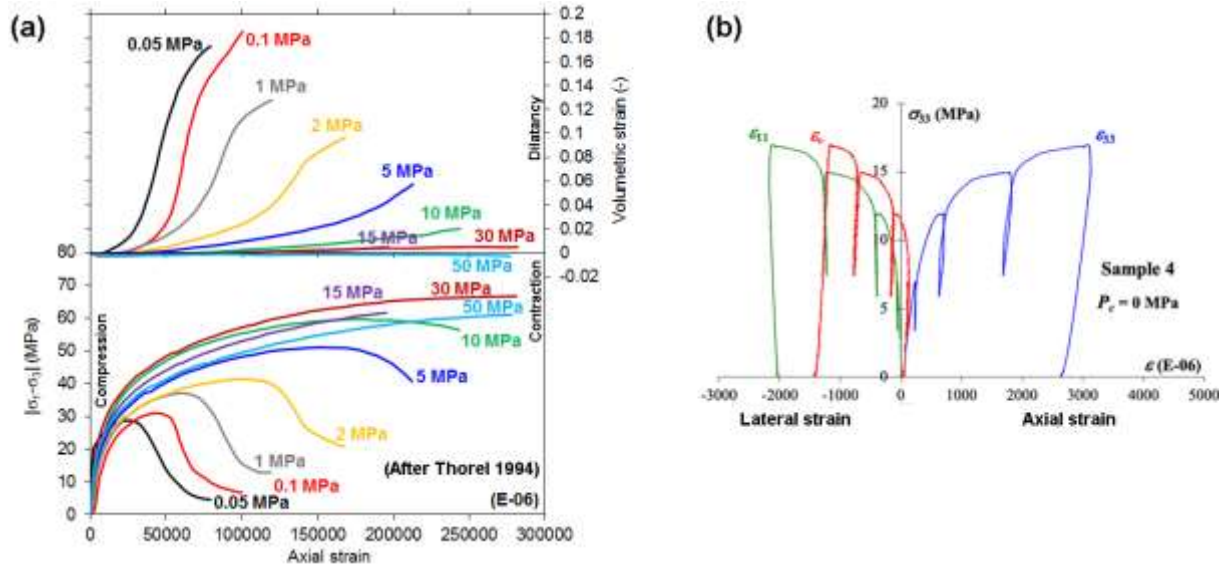


Figure 1.- (a) Deviatoric stress–axial strain curves of rock salt under different confining pressures (Thorel 1994); (b) stress–strain curves of an uniaxial compression tests on rock salt (Grgic et al. 2022).

- The initially isotropic rock salt exhibits a slight induced anisotropic damage (Grgic et al. 2022). For the sake of simplicity, we consider that the instantaneous damage is isotropic, modifies both strength and elastic properties of rock salt, as well as initiates from the dilatancy threshold.
- Experimental creep tests of rock salts show that they exhibit a transient phase in which the creep strain rate reduces significantly due to the strain hardening, a stationary phase in which the creep strain rate remains constant and an acceleration phase in which the creep strain rate shows a rapid increase due to micro-cracks growth and damage propagation. The latter phase can only occur if the stresses are above the instantaneous (short-term) dilatancy threshold (Hunsche and Hampel 1999), leading to increased damage until long-term failure (or creep rupture) is reached. The short-term dilatancy threshold is similar to the long-term dilatancy threshold (Hunsche and Hampel 1999). Furthermore, the occurrence of tertiary creep and creep rupture tends to be suppressed by the application of high confining pressure (Fossum et al. 1993). In this

work, the long-term behaviour model considers the three creep regimes (transient, stationary and acceleration). In tertiary creep, damage is considered to cause the rapid increase in the creep strain rate.

- Dynamic (i.e., cyclic) mechanical fatigue induces micro-cracking damage in rock salt (Liu et al. 2014; Grgic et al. 2022). The axial compressive strength of rock salt decreases as the number of loading cycles increases (Guo et al. 2012). On the other hand, self-healing can restore hydromechanical properties of damaged rock salt but not to the initial state (Chen et al. 2013). In this work, neither the effects of dynamic fatigue nor the self-healing mechanism is taken into account.
- Weak hydromechanical coupling as observed by Grgic et al. (2022) (an almost zero value is considered for the Biot coefficient even though it increases slightly with rock salt damage).
- Experimental laboratory tests have shown that the evolution of permeability initiates approximately at the dilatancy threshold and increases with the evolution of dilatancy (Popp et al. 2007, Grgic et al. 2022). Furthermore, with the increase of confining pressure, which causes the closure of voids, a decrease in permeability is induced (Popp et al. 2001; Grgic et al. 2022). In contrast, long-term permeability measurements reveal a decrease in permeability due to the self-healing mechanism (Peach 1991; Grgic et al. 2022). In dynamic fatigue test, no significant increase in permeability was found (Grgic et al. 2022). In this work, we consider the evolution of dilatancy by means of instantaneous damage. This damage, which takes into account the effect of confining pressure, affect the intrinsic permeability of rock salt. Concerning the long-term behaviour, we do not consider the modification of permeability induced by tertiary damage due to the lack of experimental data.
- In the short-term, high temperature can reduce the maximum resistance as well as change the rock salt behaviour from brittle to ductile (Wawersik and Hannum 1980). In the long-term, rock salt ductility also increases with increasing temperature. In this work, the effect of temperature is not taken into account even though strong temperature variations are expected inside the cavern: the model remains isothermal.
- In the absence of thermal coupling, the stress state around the salt cavern is in compression, so the short-term behaviour model is limited to this regime only.

2.2. Short-term behaviour

The current state-of-the-art (e.g., Salzer et al. 2015; Liu et al. 2020), in particular based on the triaxial compression tests performed by Thorel (1994) and Grgic et al. (2022) on the same rock salt, indicate that the main mechanical characteristics of the short-term behaviour may be summarised as follows: a very short linear elastic phase; a hardening phase with plastic

deformation and diffuse damage; a transition from quasi-brittle to ductile behaviours with the increase in confining pressure; a negligible volumetric dilatancy at high confining pressure. The recent test results of Grgic *et al.* (2022) up to the investigated axial deformation of 0.4%, reveal that the studied rock salt remains governed by strain hardening mechanism. Consequently, the quasi-brittle behaviour or strain softening observed for low confining pressures will not be considered in the proposed model.

Hereafter, we consider that the compressive stresses are negative and that the principal stresses follow the convention $\sigma_1 \geq \sigma_2 \geq \sigma_3$. Inspired by the well-known Mohr-Coulomb criterion expressed in terms of the three stress invariants (p, q, θ), an elastoplastic and instantaneous damage criterion is proposed as follows:

$$f_p(\boldsymbol{\sigma}, \gamma_p, d_i) = q + p M_p - N_p$$

$$M_p = \eta^p(\gamma_p) \frac{\sin \phi}{\left(\frac{\cos \theta}{\sqrt{3}} - \frac{1}{3} \sin \theta \sin \phi\right)} ; \quad N_p = \eta^p(\gamma_p) \frac{(1 - d_i) c \cos \phi}{\left(\frac{\cos \theta}{\sqrt{3}} - \frac{1}{3} \sin \theta \sin \phi\right)} \quad (1)$$

where the means stress p , the equivalent (von Mises) deviatoric stress q and the Lode angle $\theta \in \left[-\frac{\pi}{6}, \frac{\pi}{6}\right]$ are expressed as follows:

$$p = \frac{\text{tr } \boldsymbol{\sigma}}{3}, \quad q = \sqrt{3J_2}, \quad \theta = \frac{1}{3} \sin^{-1} \left(\frac{-3\sqrt{3} J_3}{2 J_2^{3/2}} \right) \quad (2)$$

with J_2 and J_3 being the second and third invariants of the deviatoric stress tensor \mathbf{s} , respectively. In Eq. (1), c and ϕ denote respectively the cohesion and the friction angle of rock salt, γ_p represents the plastic distortion (i.e., the equivalent shear plastic strain), d_i is the instantaneous damage variable and η^p describes the plastic hardening. It is worthy to emphasize that the yield profile upon the deviatoric stress plane described by the Lode angle θ together with q allows us to differentiate the yield surfaces of compressive stress paths from those in extension.

Moreover, based on the work of Zhou *et al.* (2011), the aforementioned hardening function $\eta^p(\gamma_p)$ can be written as:

$$\eta^p(\gamma_p) = \eta_o^p + \{1 - \eta_o^p\} \frac{\gamma_p}{\alpha^p + \gamma_p} \quad (3)$$

where η_o^p represents the elastic limit being defined by a fraction of the peak strength ($\eta^p = 1$). The parameter α^p controls the plastic hardening rate.

Furthermore, it is well known in geomechanics, that the transition from contractant to dilatant behaviour is usually characterised by using a non-associated plastic flow rule. This indicates

that the dilatancy angle is different from the internal friction angle (of the yield surface), and so the plastic flow develops in a direction different from that normal to the yield surface. The dilatancy angle is generally smaller than the friction angle, especially for cohesive and frictional materials such as geomaterials. Regarding our specific rock salt, as it can be understood that almost no dilatation occurs under high values of confining pressure (e.g. values larger than 10 MPa), which consequently leads to a prevailing contractant behaviour, the non-associated flow rule is adopted by referring the work of Chiarelli et al. 2003 (see also Souley et al. 2022):

$$g(\boldsymbol{\sigma}, \gamma_p) = q + \beta(\gamma_p) p \quad (4)$$

with $\beta(\gamma_p)$ being the dilatancy coefficient defined as:

$$\beta(\gamma_p) = \begin{cases} \beta_m - (\beta_m - \beta_0)e^{-b\beta\gamma_p} & ; \gamma_p < \gamma_{ult} \\ \beta_{ult} \exp\left(1 - \frac{\gamma_p}{\gamma_{ult}}\right) & ; \gamma_p \geq \gamma_{ult} \end{cases} \quad (5)$$

where β_0 ($\beta_0 < 0$) is the initial volumetric contraction, β_m ($\beta_m > 0$) is the volumetric dilatancy at large deformation (and under low to moderate confining pressures) and β_{ult} ($\beta_{ult} = \beta_m - (\beta_m - \beta_0)e^{-b\beta\gamma_{ult}}$) is the maximum volumetric dilatancy reached at the plastic distortion γ_{ult} ($\gamma_{ult} > \gamma_p^*$). γ_p^* is the plastic distortion threshold of instantaneous damage initiation, which will be defined later. This plastic potential described by Eqs. (4) and (5) introduces a volumetric contraction when $\beta < 0$, whereas the plastic strains evolve towards volumetric dilatancy if $\beta > 0$. Note that since the volumetric dilatancy does not grow indefinitely as shown by experimental results (Figure 1a - up), in the case of large deformations, the dilatancy coefficient decreases progressively towards zero from the ultimate plastic deformation (γ_{ult}) in Eq. (5) to stop the increase in volumetric dilatancy. Moreover, in order to take into account the reduction of volumetric dilatancy with increasing confining pressure, β_m is heuristically expressed as an exponential function of the parameter (a_p) describing the relative effect of confining pressure, the maximum dilatancy coefficient under uniaxial compressive conditions (β_{m0}) and the major principal stress (σ_1):

$$\beta_m = \begin{cases} \beta_{m0} \exp(a_p \sigma_1) & ; \sigma_1 < 0 \\ \beta_{m0} & ; 0 \leq \sigma_1 \end{cases} \quad (6)$$

From the dilatancy coefficient and the condition of instantaneous damage initiation $\beta(\gamma_p^*) = 0$, it is possible to determine the value of the plastic distortion threshold for instantaneous damage initiation, which reads: $\gamma_p^* = -\frac{1}{b\beta} \ln\left(\frac{\beta_m}{\beta_m - \beta_0}\right)$. Using this plastic distortion value and Eq. (1), the damage threshold ($f_{ds} = 0$) can then be computed as follows:

$$f_{ds} = q + pM_{ds} - N_{ds} \quad (7)$$

where $M_{ds} = M_p(\gamma_p^*)$ and $N_{ds} = N_p(\gamma_p^*)$. This damage threshold would correspond to the previously mentioned dilatancy threshold found in the rock salt literature.

Next, let us come to the instantaneous damage description of the studied rock salt. It is widely accepted that rock dilatancy is a relevant indicator of damage (Bérest 2013). Experimental results (Popp et al. 2001; Liang et al. 2011) show that after the material has undergone volumetric dilatancy due to micro-cracking, a modification of both strength capacities and transport properties is observed. An exponential description is used to determine the isotropic instantaneous damage (d_i) based on continuous damage mechanics, which reads:

$$f_d = d_{max}\{1 - \exp(-b_d(Y_d - Y_0))\} - d_i \leq 0 \quad (8)$$

Eq. (8) is based on the work of Mazars (1984) on the concrete materials modelling, where $Y_d = \sqrt{\langle \boldsymbol{\varepsilon} \rangle : \langle \boldsymbol{\varepsilon} \rangle}$ is the thermodynamic force conjugated to the instantaneous damage field d_i . This force is expressed as a function of the positive principal strain tensor $\langle \boldsymbol{\varepsilon} \rangle$, where $\langle . \rangle$ is the Macauley bracket and $\boldsymbol{\varepsilon}$ is the total principal strain tensor. Y_0 is a material constant describing the initial state of Y_d at $\beta(\gamma_p^*) = 0$, b_d denotes the growth rate of the instantaneous damage, d_{max} represents the maximal instantaneous damage reached at the peak strength. It is worthy to point out here that since the volumetric strains are considered contractant under high confining pressures, fracturing cannot be initiated. Following (Zhou et al. 2011), the maximal instantaneous damage is written as:

$$d_{max} = \begin{cases} d_{max0} \exp(a_d \sigma_1) & ; \sigma_1 < 0 \\ d_{max0} & ; 0 \leq \sigma_1 \end{cases} \quad (9)$$

where a_d is the parameter describing the effect of confining pressure on d_{max} , d_{max0} is the maximal instantaneous damage reached under uniaxial compressive conditions and σ_1 is the major principal stress. In the present work we assume that the effect of confining pressure on the decrease in volumetric dilatancy and on the decrease in instantaneous damage is the same. Therefore, for the sake of simplicity, we consider $a_d = a_p$.

2.3. Long-term behaviour

The long-term behaviour of rock salt is characterised by creep even under very small deviatoric stresses. Under constant deviatoric loading, this material exhibits three distinct stages which can be observed in creep tests: (i) transient (i.e. primary) creep in which the strain rate decreases due to the strain hardening or time hardening; (ii) steady-state (i.e. secondary) creep in which the strain rate remains constant; and (iii) accelerated (i.e. tertiary) creep in which the strain rate shows a rapid increase due to delayed rupture. Furthermore, experimental results from uniaxial and triaxial compressive creep tests show that the creep strain rate increases with the deviatoric stress at constant confining pressure (Yang et al. 1999). Creep in rock salt is also temperature-dependent, however in this work, isothermal conditions are assumed, as mentioned above.

The long-term behaviour is simulated through a viscoplastic model inspired by some pioneering works describing either the transient phase or the steady-state phase, or both (Cristescu 1993; Heusermann et al. 2003). More precisely we adopt herein a stepwise decomposition of the non-linear creep deformation. The deformation mechanisms of the three creep phases are still active but with varying intensity. The transient phase is described mainly by the contribution of the Kelvin model and is expressed as a function of primary creep strain hardening ε_{tr} (Heusermann *et al.* 2003). The stationary phase is represented by the Norton law as widely adopted in rock salt modelling (e.g., Shahmorad et al. 2016). Thus, the increase in creep deformation is written as:

$$\dot{\varepsilon}^c = \left(\frac{1}{\bar{\eta}_k^*} (q^* - \bar{G}_k^* \varepsilon_{tr}) + A_N \left(\frac{q^*}{\sigma_{ref}} \right)^{n_N} \right) \frac{3}{2} \frac{\mathbf{s}}{q^*} \quad (10)$$

where $\bar{G}_k^* = G_k \exp(k_1 q^*)$; $\bar{\eta}_k^* = \eta_k \exp(k_2 q^*)$; n_N is the dimensionless exponent and A_N is the Norton viscosity at the reference temperature, and σ_{ref} is the reference equivalent deviatoric stress.

In order to consider tertiary creep, the undamaged equivalent deviatoric stress has been modified as follows: $q^* = \frac{q}{1-d_t}$, where d_t is the tertiary damage that is activated when the stresses are in the dilatancy zone, defined between the damage threshold and the peak strength. This means that tertiary creep is occurring when stresses exceed the damage threshold, as experimentally observed (Hunsche and Hampel 1999). Tertiary damage is assumed to be independent of instantaneous damage. Based on the work of Hou (2003), the tertiary damage rate is written as follows:

$$\dot{d}_t = A_T \frac{\left(\frac{f_{ds}}{\sigma_{ref}} \right)^{n_T}}{(1-d_t)^{n_T}} \quad (11)$$

where f_{ds} is the damage threshold, n_T and A_T control the tertiary damage rate increase. Thus, tertiary damage may only be activated and enlarged if the stresses exceeded the damage threshold. Eq. (11) can be solved under the condition of monotonic creep condition and assuming that $d_t(t=0) = 0$. Thus, the tertiary damage evolution is given by:

$$d_t = 1 - \left[1 - A_T (1 + n_T) \left(\frac{f_{ds}}{\sigma_{ref}} \right)^{n_T} t \right]^{\frac{1}{1+n_T}} \quad (12)$$

2.4. Hydromechanical coupling and damage-induced permeability changes

Considering a fully water-saturated material, the main equations of the hydromechanical problem are:

$$\begin{aligned} \vec{\nabla} \cdot (\tilde{\mathbb{C}}^e : \boldsymbol{\varepsilon}^e - b p_f \mathbf{I}) + \vec{f} &= 0 \\ \rho_f b \frac{\partial \varepsilon_v}{\partial t} + \frac{\rho_f}{M} \frac{\partial p_f}{\partial t} + \vec{\nabla} \cdot (\rho_f \vec{q}) &= 0 \end{aligned} \quad (13)$$

where $\tilde{\mathbb{C}}^e = (1 - d_i - d_f)\mathbb{C}^e$ is the fourth-order drained elasto-damaged stiffness tensor, \mathbb{C}^e is the fourth-order drained elasticity stiffness tensor, d_i is the instantaneous damage variable, d_t is the tertiary damage variable, $\boldsymbol{\varepsilon}^e$ is the elastic strain tensor, \vec{f} is the volume force, ε_v is the volumetric strain, p_f is the fluid (pore) pressure, \mathbf{I} is the second order identity tensor, $\vec{\nabla}$ is the nabla operator, \vec{q} is the fluid volumetric flux vector, b and M are the Biot coefficient and Biot modulus respectively. The Biot coefficient for rock salt is very close to zero according to Grgic *et al.* (2022) and can reach a maximum of 0.15 after damage, while Zhang *et al.* (2020) indicate a upper value of 0.36. But both authors agree that this coefficient increase is a consequence of the dilatancy of the material and, subsequently, of the damage. In this work, we consider an initial value equal to the porosity value: 0.012 (i.e., weak hydromechanical coupling for intact rock salt) but once the instantaneous damage initiates, b may increase up to a value of 0.3 through a smoothed step function. For an ideal and isotropic porous material, the Biot modulus is given by:

$$\frac{1}{M} = \frac{n}{K_f} + \frac{(1-b)(b-n)}{K_d} \quad (14)$$

where n is the porosity, K_f and K_d are respectively the fluid compression modulus and the drained compressibility modulus of the porous medium. According to Darcy's law, the fluid flow is given by:

$$\vec{q} = -\frac{k}{\mu_f} (\vec{\nabla} p_f + \rho_f \vec{g}) \quad (15)$$

where k is the permeability, μ_f is the dynamic viscosity of the fluid, ρ_f is the fluid density and \vec{g} is the gravity. The values of ρ_f and μ_f are constant since hydrogen solubility is very low.

Regarding the evolution of permeability in rock salts, numerous experimental investigations (Peach and Spiers 1996; Schulze et al. 2001; Popp et al. 2001; Alkan et al. 2007; Grgic et al. 2022) indicated an increase in permeability when the deviatoric stress exceeds the dilatancy threshold. The increase in permeability can be more than four orders of magnitude compared to the initially undisturbed sample. The evolution of isotropic permeability in rock salt is classically expressed as a function of porosity (Stormont 1997; Popp et al. 2007), volumetric strain (Peach and Spiers 1996), as well as a combination of confining pressure and porosity/volumetric strain (Stormont et al. 1992; Popp et al. 2007). In this work, since the instantaneous damage variable represents the modification of the mechanical characteristics

of the material, this parameter is also assumed to drive the changes in permeability. Therefore, the empirical model of Gawin et al. (2002) is used :

$$k = k_0 10^{A_k d_i} \quad (16)$$

where k_0 is the intrinsic permeability of the intact material, A_k is a model parameter and d_i is the instantaneous damage. Eq. (16) indicates that the more damaged the material is, the higher the permeability. Since the instantaneous damage in the model increases more at low confining pressures, permeability will be subject to higher changes for such confining pressures. This feature is consistent with the experimental results of Popp et al. (2007). Intrinsic permeability of intact (i.e., undamaged) rock salt is very low and, in general, values can be lower than 10^{-21} m^2 (Peach 1991; Stormont 1997; Cosenza and Ghoreychi 1999). In our case, a value of 10^{-20} m^2 is considered as initial value. The A_k parameter is calibrated using the experimental results of Schulze *et al.* (2001) at confining pressure of 2 MPa (Figure 2a). A good calibration of the permeability-strain curve (Figure 2b), with an increase up to five orders of magnitude, is obtained with this value of confining pressure. In contrast, when 5 MPa of confining pressure is simulated, the increase in permeability is only one order of magnitude. Experimentally, it has been observed that indeed, increasing the confining pressure causes a decrease in microcracking damage and, therefore, a decrease in permeability (Popp et al. 2007; Grgic et al. 2022).

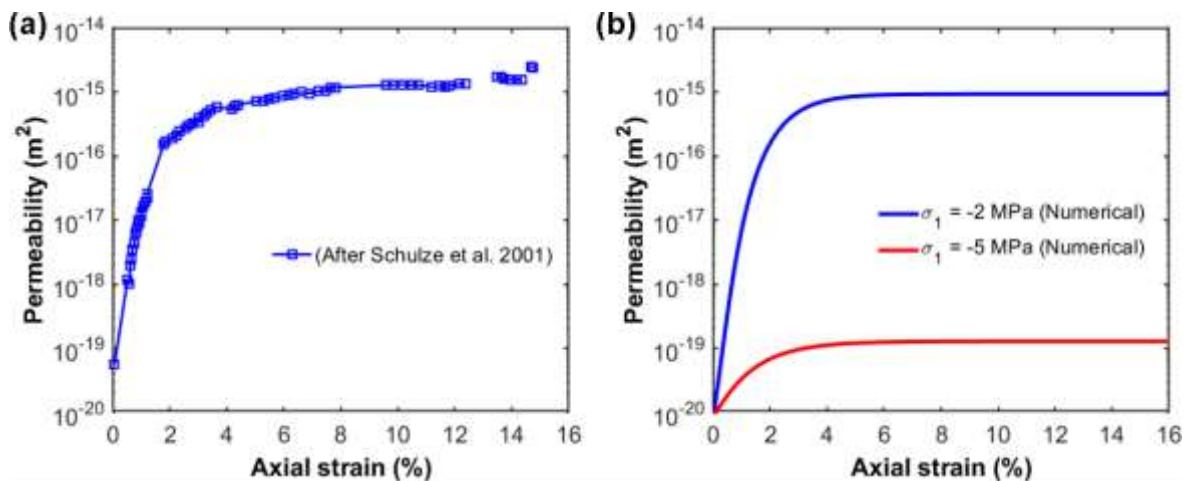


Figure 2.- Permeability versus axial strain curves of (a) the triaxial compression test (Schulze et al. 2001) at confining pressure of 2 MPa, and (b) the numerical results at confining pressures of 2 MPa and 5 MPa.

In addition to the hydromechanical modelling, an analysis of the hydrogen extent within the rock mass is carried out. Since water and hydrogen are immiscible, we assume hereafter that the threshold capillary pressure of rock salt is much higher than hydrogen pressure within the cavern due to the nanometric size of pore throats and hence no free gas phase will be flowing. Assuming hydrogen is a non-reactive solute (no chemical reaction or sorption with salt), we

use the following mass transport equation to delineate the extent and mass of dissolved hydrogen plume. Transport of dissolved H₂ is only driven by advection (Darcy's law) and by diffusion, since mechanical dispersion is negligible due to the low permeability of the porous medium.

$$n \frac{\partial(c_{H_2})}{\partial t} + \vec{\nabla} \cdot (\vec{q} c_{H_2}) = \vec{\nabla} \cdot (n D^* \cdot \vec{\nabla} c_{H_2}) \quad (17)$$

where c_{H_2} is the hydrogen concentration, n is the porosity and D^* is the diffusion coefficient of hydrogen in water. Concentration values c_{H_2} will be presented dimensionless in the following section for the sake of simplicity.

3. Numerical modelling

3.1. Model verification and validation from triaxial test path

The proposed constitutive model is applied to analyse triaxial tests at different confining pressures, with the objective, in first instance, of verifying the short-term response. The model parameters are listed in **Erreur ! Source du renvoi introuvable.** We combine experimental data of Thorel (1994) and Grgic *et al.* (2022) for model calibration purpose. More specifically, elastic and strength parameter values are fitted from Thorel (1994), while the plastic potential and hardening parameters are calibrated mainly from Grgic *et al.* (2022). As an example, **Erreur ! Source du renvoi introuvable.**a shows the numerical results of a cyclic uniaxial compression test. The volumetric strain (in red) reproduces adequately the contractant and dilatant behaviour observed experimentally. As for the axial and radial strains, the mismatch is due to using a strain hardening that matches well with the results of both Thorel (1994) and Grgic *et al.* (2022), both of which have different measured strain hardenings. Indeed, although both studies examined the same rock salt formation, they exhibited distinct rheological features, resulting in some differences in the mechanical characteristics. In **Erreur ! Source du renvoi introuvable.**b, the instantaneous damage response shows plateaus corresponding to the different unloading-reloading cycles, which indicates that the accumulated instantaneous damage is not reversible.

Another simulation is carried out from Thorel (1994) experimental tests. For this purpose, confining pressures of 0.05, 0.1, 1, 2, 5 and 10 MPa are considered, under which deviatoric loads are applied until axial strains of 8%, 10%, 12%, 17%, 20% and 20%, respectively. The numerical results provided by the model are compared with the experimental data in Figure 4. Although the strain hardening is fast compared to the experimental results, there is a satisfactory agreement between the experimental and numerical values for peak strengths (Figure 4a and b). On the other hand, the maximum numerical values of volumetric strain (Figure 4d) are lower than the experimental data. That is because the plastic potential

parameters were calibrated mainly from the experimental tests of Grgic *et al.* (2022), i.e., for relatively small deformations compared to Thorel (1994). Consequently, the model predicts that the volumetric strain begins to be dilatant at small deformations and its growth rate is almost constant, whereas Thorel (1994) observes that the dilatancy occurs at slightly larger deformations and the growth rate increases rapidly. Figure 4c shows the model capability to reproduce the decrease of volumetric dilatancy with increasing confining pressure. Numerical results are compared with the theoretical solutions of the Mohr-Coulomb criteria at the elastic limit, damage threshold, and peak strength in Figure 5a. There is a good agreement for all the levels of confining pressure. The model also shows the evolution of the instantaneous damage. This one increases with the axial strain until reaching its limit damage value, which reduces with increasing confining pressures (Figure 5b). Finally, based on this comparison with the aforementioned theoretical solutions and experimental results, the elastoplastic and instantaneous damage model is considered to be verified.

Table 1.- Values used in the hydromechanical simulations. Short- and long-term model parameters.

Mechanical parameters								
Elastic model			Short-term model			Long-term model		
E	35	GPa	c	8	MPa	k_1	-0.18	1/MPa
ν	0.3		ϕ	36.8	°	G_k	126000	MPa
ρ_s	2100	kg/m ³	η_o^p	0.35		k_2	-0.15	1/MPa
			α^p	0.0024		η_k	60000	MPa.d
			β_0	-0.02		A_N	1.31E-09	1/d
			β_{m0}	1.1		n_N	4	1/d
			b_β	350		σ_{ref}	1	MPa
			γ_{ult}	0.09		A_T	4 E-08	1/d
			d_{max0}	0.15		n_T	5	
			b_d	100				
			a_d	0.5	1/MPa			
Hydraulic parameters								
k_0	1E-20	m ² /s	n	0.012 ⁽¹⁾		ρ_f	1000	kg/m ³
A_k	90		b	0.012 ⁽¹⁾				
μ_f	0.001	Pa.s	K_f	2.2E+09	Pa			
Transport parameters (dissolved hydrogen)								
D^*	6E-09	m ² /s						

⁽¹⁾ (Grgic *et al.* 2022)

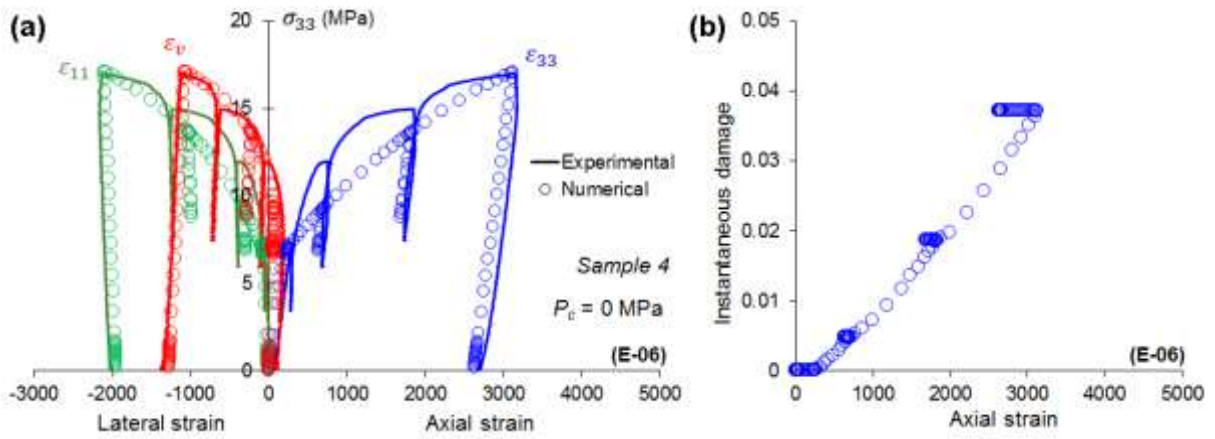


Figure 3.- (a) Comparison of stress-strain curves of uniaxial compression test (experimental results on sample 4 from Grgic *et al.* 2022), and (b) numerical curve of instantaneous damage versus axial strain.

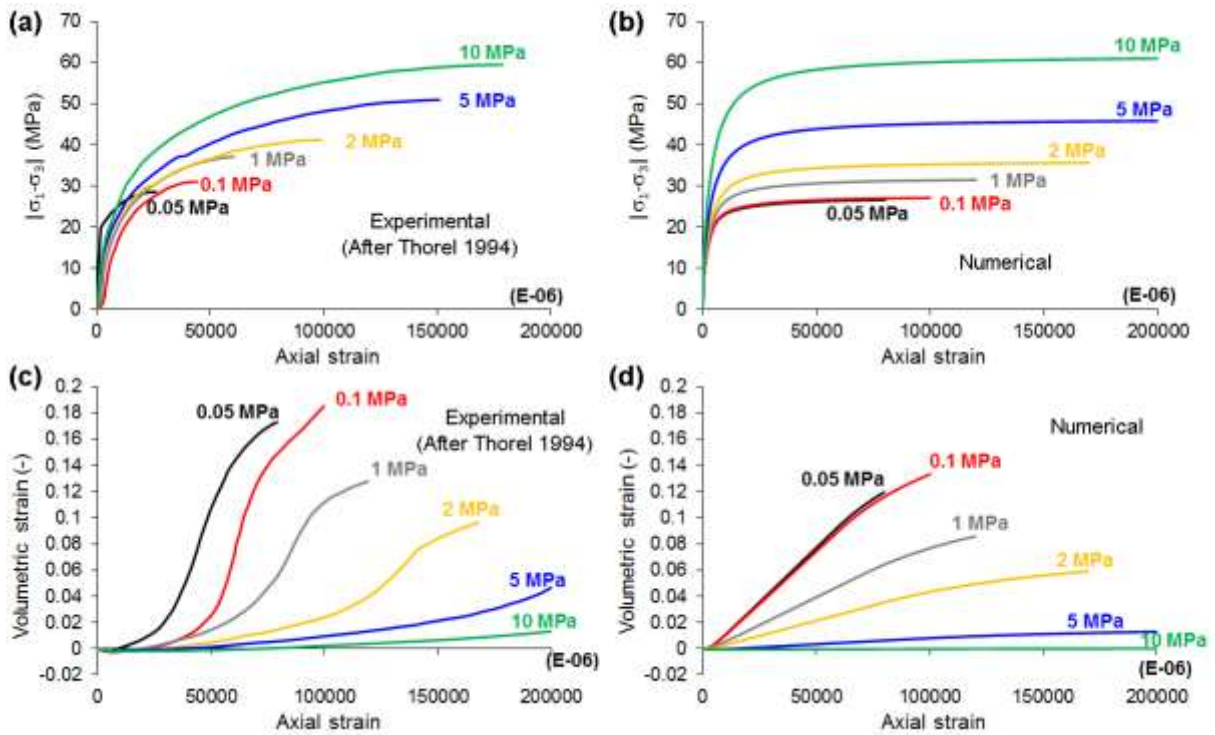


Figure 4.- (a) - (b) deviatoric stress versus axial strain curves, and (c) - (d) volumetric strain versus axial strain curves. The values next to the curves correspond to the confining pressures in absolute value.

In a second instance, we assess the long-term response of the model. Uniaxial creep tests over a period of 60 days are analysed. Axial loads of 6, 12 and 18 MPa are applied. The long-term properties are given in **Erreur ! Source du renvoi introuvable.** The evolution of the creep deformation is illustrated in Figure 6a. We carried out simulations with and without activating tertiary creep model (dotted line versus continuous line curves in Figure 6a). It can be observed that the primary and secondary creeps occur when $q = 6$ MPa, whereas a tertiary

creep is triggered when the deviatoric load exceeds a certain damage threshold (i.e., $q = 7.4$ MPa in this numerical simulation). It should be noted that the evolution of tertiary damage is not simulated here until the creep failure. At the 18 MPa load, the increase in tertiary damage variable, as predicted by (Eq. 12), accelerates the creep deformation (Figure 6b). These results are consistent with the theoretical criteria, as shown in Figure 5a where it can be observed that the loads of 12 and 18 MPa are in the dilatancy zone and therefore the tertiary damage variable is different from zero.

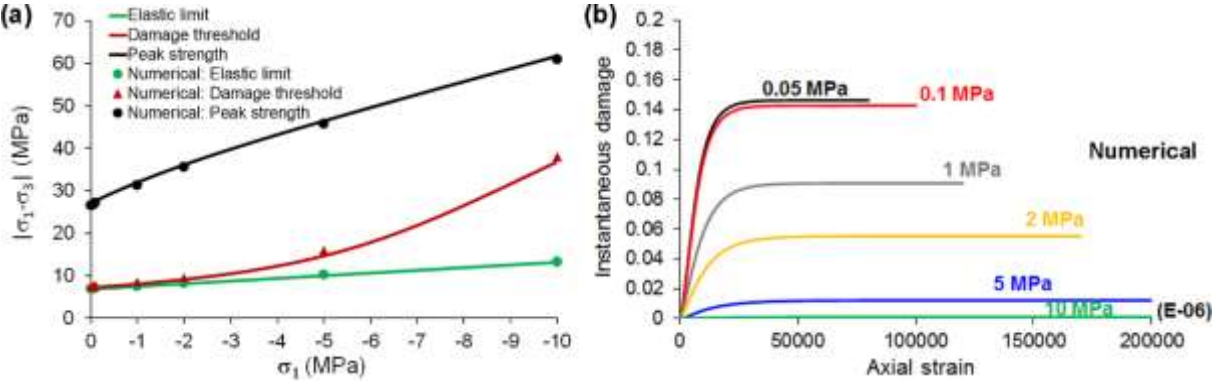


Figure 5.- (a) Comparison of model result and theoretical criteria and (b) instantaneous damage versus axial strain curves. The values next to the curves correspond to the confining pressures in absolute value.

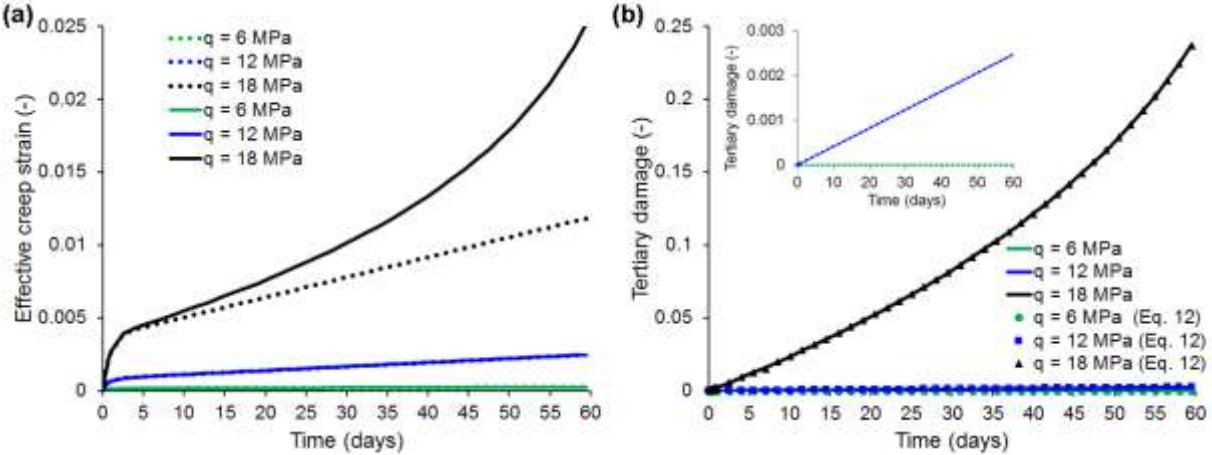


Figure 6.- (a) Effective creep strain versus time curves and (b) tertiary damage versus time curves. Dotted line: the model considers only primary and secondary creep. Continuous line: full creep model.

3.2. Hydromechanical modelling of cavern: case study

3.2.1. Cavern geometry, boundary and initial conditions and properties

Currently, there are only a few sites for hydrogen storage in salt caverns (Caglayan et al. 2020). The oldest one is located in the United Kingdom, with three adjacent caverns in the Teesside salt fields. Each cavern has a relatively small volume ($70\,000\text{ m}^3$), an elliptical shape and is located at an average depth of 350 m. They have been in operation since the 1970s. In contrast, one of the largest caverns is in the Spindletop salt dome, in Texas (US). This

hydrogen storage cavern, operated by Air Liquide since 2014, has a total volume of 906 000 m³ characterized by quite regular cylindrical shape, and an average depth of 1350 m.

These two types of caverns are used as representative cases of underground hydrogen storage. For sake of simplicity, we will consider a single cavern for both cases which means that the cavern group will not be modelled. The shape of each cavern is cylindrical with half-spheres at the top and bottom. The shallow cavern (-350 m) has a volume of 70 686 m³, a diameter of 30 m, and a height of 110 m. The very deep cavern (-1350 m) has a volume of 910 800 m³, a diameter of 70 m, and a height of 260 m. The same height/diameter ratio of 3.7 is considered for both caverns, making deep cavern homothetic to shallow cavern by approximately 13 times.

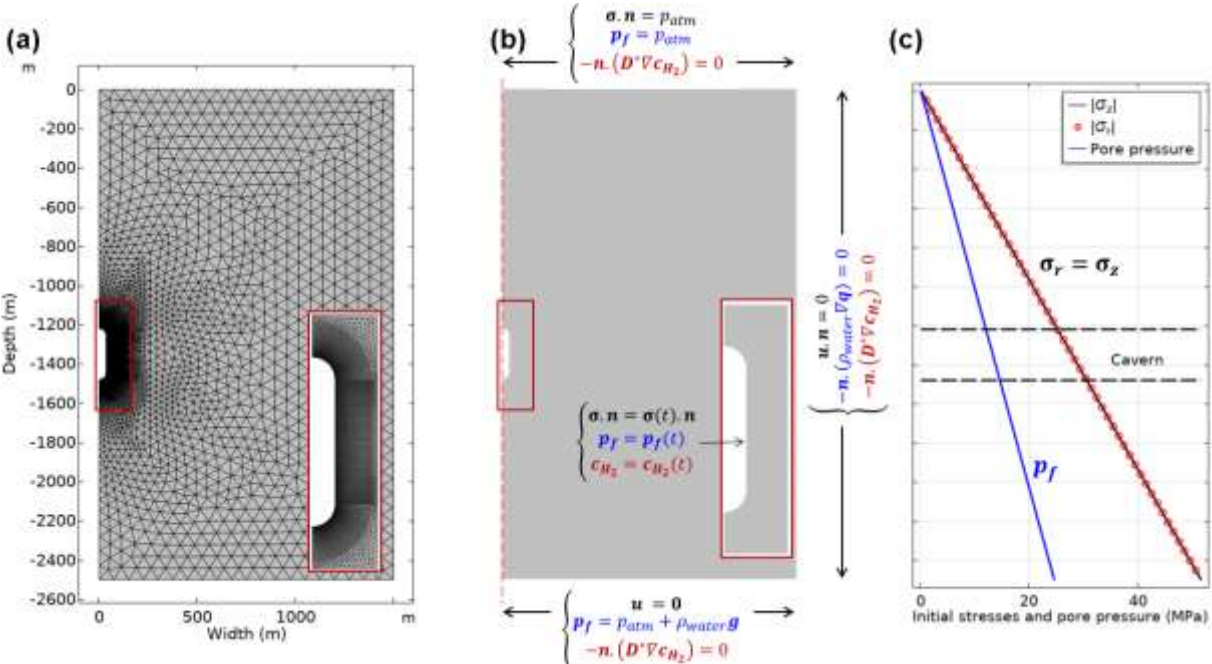


Figure 7.- (a) Geometry and mesh around the deep cavern; (b) axisymmetric model and boundary conditions; (c) initial hydromechanical conditions.

A fully coupled hydromechanical formulation is used to calculate the displacements and pore pressure based on Eq. 13. This pressure mixed formulation (also known as *u-p* formulation) takes into account the coupling between the displacement and pore pressure fields, enabling a more precise representation of the interactions between solid deformation and fluid flow in both directions. To numerically solve the coupled equations, the Newton-Raphson method, a widely-used iterative technique for solving nonlinear systems of equations, is utilized. The displacements are solved using a Lagrangian quadratic shape function, while the pore pressure is solved using a Lagrangian linear shape function. A mesh convergence study has

been conducted to optimize the mesh size, resulting in a fine mesh with 17183 triangular elements.

The 2D radial geometry, mesh, initial and boundary conditions are illustrated in Figure 7 for the deep cavern. The initial pore pressure is equal to the geostatic pore pressure, while the in-situ stresses are isotropic and equal to the overburden pressure. On the top, constant atmospheric pressure and free normal stress boundary conditions are applied. On the right side, there are no horizontal displacements and no-flow boundary. On the bottom, displacements are fixed to zero. On the left side, there is axisymmetric condition, while on the cavern wall there are applied stresses and pore pressure. Regarding the transport equation, a constant hydrogen concentration is imposed on the cavern wall and a zero-flux boundary condition everywhere else. The hydromechanical properties used are listed in **Erreur ! Source du renvoi introuvable.**

3.2.2. Excavation and operational phases

The following phases are considered in hydromechanical simulations (Figure 8):

Phase 1: *Initial state.* There is no salt cavern ($t=0$). In this phase, the initial geostatic stresses prior to the cavern excavation, are determined.

Phase 2: *Leaching.* The salt cavern is excavated by solution mining technique. The initial stresses inside the cavern are gradually replaced by the brine pressure (Point 1 in Figure 8). The density value of the brine used is 1100 kg/m^3 . The duration of this phase is assumed to be one year ($t=1 \text{ year}$).

Phase 3: *Brine.* The cavern is filled with brine, so brine pressure is applied to the cavern wall (from points 1 to 2 in Figure 8). This phase is considered to last another year ($t=2 \text{ years}$).

Phase 4: *Debrining.* Hydrogen injection, and gradual replacement of the brine, is carried out. The considered duration of this phase is 6 months ($t=2.5 \text{ years}$), during which 100% of the maximum hydrogen pressure is reached (Point 3 in Figure 8). The internal pressure (pressure inside the cavern) increases due to the replacement of brine pressure by hydrogen pressure. Neglecting the capillary pressure jump between hydrogen and water, we assumed that the pore pressure value on the cavern wall is equal to the hydrogen pressure value inside the cavern. Thus, in the hydrogen mass transport, the solubility concentration $c_{H_2} = 1$ (in dimensionless form) applies to the cavern wall.

Phase 5: *Cycling loading operation.* After considering 6 months of maximum hydrogen pressure ($t=3 \text{ years}$), hydrogen injection and withdrawal cycles are performed considering a sinusoidal waveform. The internal pressure (hydrogen pressure in this phase) at the cavern is reduced to the minimum operating pressure. Two scenarios are analysed (Figure 9): (i) seasonal and (ii) daily. The seasonal scenario corresponds to the classical operating

conditions, where gas is withdrawn during winter, when the demand is highest. This modelling scenario, considers 6 months of withdrawal and 6 months of injection, during 50 years of activity ($t= 53$ years). Conversely, the daily scenario simulates a more aggressive operational mode, with typical expected variations in renewable power generation and energy demand (Ineris 2022). This scenario considers 4 hours of extraction, 6 hours of injection, another 4 hours of extraction and, finally, 10 hours of injection, so there are two cycles in one day. The operating time considered is 100 days ($t= 3$ years + 100 days). The maximum and minimum hydrogen pressure values vary for both scenario between 70%-80% and 20%-30% of the initial geostatic pressure, respectively. The values of the maximum and minimum hydrogen pressures for the shallow cavern are respectively 5 and 2 MPa, while for the deep cavern they are respectively 20 and 6 MPa. Cyclic changes in hydrogen pressure are used in the hydromechanical modelling but the c_{H_2} value is kept constant during all the simulations (the changes in H_2 solubility with pressure are neglected).

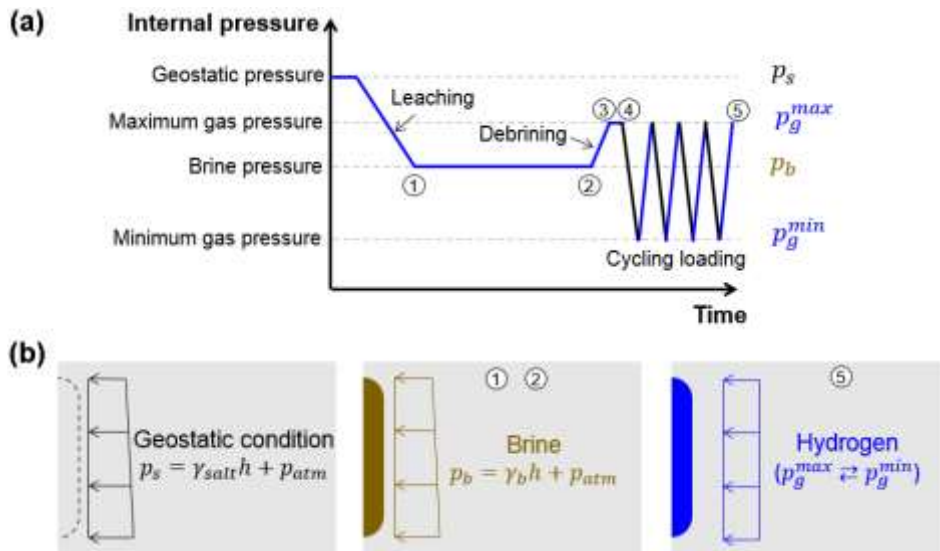


Figure 8.- (a) Internal pressure of the cavern in time and (b) schematization.

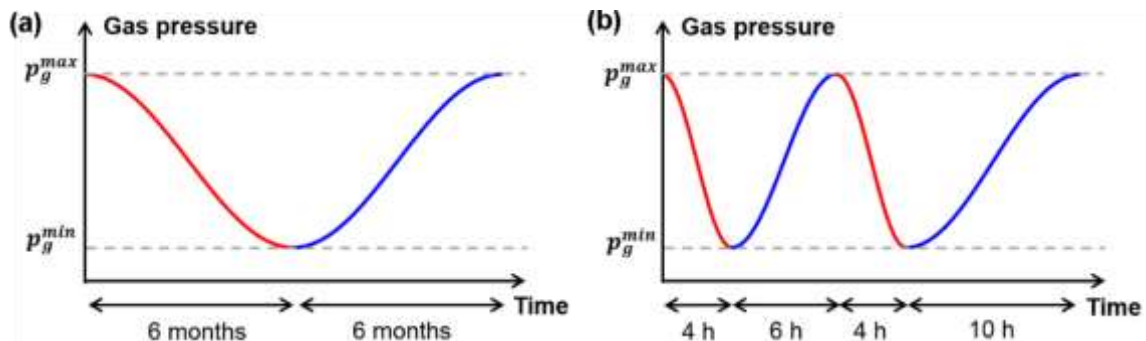


Figure 9.- Cycling scenarios: (a) seasonal and (b) daily.

3.3. Shallow versus deep cavern

This section compares the hydromechanical responses of the shallow and deep caverns.

3.3.1. Mechanical response

The stress paths at the bottom of the cavern during all loading phases are represented in Figure 10. The excavation of the cavern, which involves modelling the change of stress on the cavern wall from initial stresses to brine pressure over a year, is carried out up to point 1. In both caverns, the stress paths do not reach the elastic limit, indicating that the behaviour remains elastic. From points 1 to 2, the internal pressure exerted by the brine on the cavern wall is maintained for a period of 1 year. During this phase, the deviatoric stress in both caverns decreases through a relaxation process. From points 2 to 3, the brine pressure is replaced by the maximum hydrogen pressure, which has a higher value. This transition occurs over a duration of 6 months. The maximum hydrogen pressure has two effects on the stress path. Firstly, it increases the effective major principal stress at the cavern wall, leading to an increase in material strength. This effect is equivalent to increasing the confining pressure in a laboratory experiment. Secondly, it decreases the deviatoric stresses around the cavern wall. As a result, the stress paths move away from the elastic limit. From point 3 to 4, the maximum gas pressure is maintained for a period of 6 months. In this phase, a slight increase in deviatoric stress is observed in both caverns, with a more pronounced effect for the deep cavern, as depicted in Figure 10c and d. The initial state of stress is disturbed locally until the rock mass attains a new state of equilibrium. Thus, it leads to an increase in deviatoric stresses on the cavern wall. From point 4, the operating cycle begins. In the case of seasonal cycling, results for the shallow cavern (Figure 10a) indicate that the elastic limit is reached during the initial gas extraction. However, for the following gas withdrawals, the stress state remains within the elastic domain. In contrast, for the deep cavern (Figure 10c), the stress path of the first gas extraction exceeds the elastic limit and reaches the damage threshold. This threshold is still slightly exceeded during the whole cycling operation. In the case of daily cycling, the stress in the shallow cavern (Figure 10b) slightly exceeds the elastic limit during the first gas withdrawal. In the following, the stress state remains similar and slightly surpasses the elastic limit. Regarding the deep cavern (Figure 10d), the behavior is similar to the one observed in seasonal cycling but the damage threshold is exceeded to a greater extent. When comparing daily and seasonal cycling, the deviatoric stress in daily cycling is higher than in seasonal cycling due to the insufficient time for stress relaxation around the cavern caused by the viscoplastic behaviour to occur. Consequently, in daily cycling, the elastic limit in the shallow cavern (Figure 10b) and the damage threshold in the deep cavern (Figure 10d) are exceeded more often and to a far greater extent than in seasonal cycling. On the other hand, the observed shift of the stress path to the left, estimated from the second cycle in the deep cavern (Figure 10c and d), is attributed to the increase in the Biot coefficient from 0.012 to 0.3. This increase leads to a decrease in effective stress.

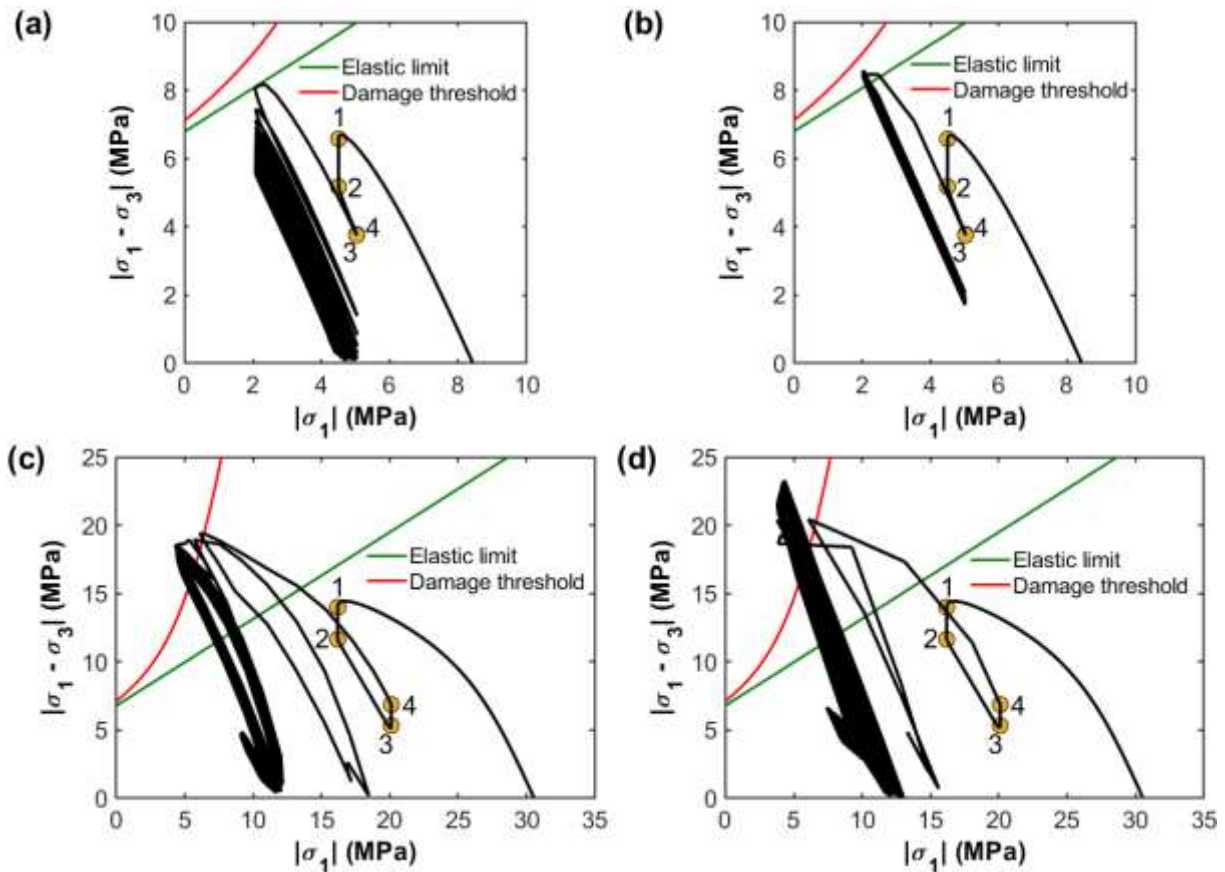


Figure 10.- Stress path at the bottom of shallow cavern: (a) seasonal and (b) daily cycling. Deep cavern: (c) seasonal and (d) daily cycling. Elastic limit and damage threshold are illustrated for Lode's angle $\theta=\pi/6$. The stresses are projected on this plane.

According to DeVries et al. (2005) and Ma et al. (2015), one of the criteria for cavern stability is that the stress state is below the dilatancy criterion, but a careful failure analysis needs also to investigate the extent of plastic and damage zones. Figure 11 shows the plastic (orange) and instantaneous damage (dark blue) zones at the end of the simulations. Around shallow cavern there is a small extension of the plastic zone on the floor and sidewall. This plastic zone is slightly more important in daily than seasonal cycling. Around deep cavern, as discussed above, a damage zone is formed, but its extension is limited to the immediate near-field of the cavern walls (approx. 2.8% cavern diameter). The plastic zone is more important and is distributed all around the cavern. The maximum extent of the plastic zone is about 31% of the diameter in seasonal cycling and 48% in daily cycling. The shape and extension of the plasticity and damage zones are similar during the first operation cycles, i.e., no change in these zones is predicted. As mentioned previously, a longer cycle duration plays role in stress relaxation due to time-dependency of this mechanism. This contributes to reduce the extent of the plastic and damage zones in seasonal cycling compared to daily cycling. In addition, in the damage zone, the stresses on the cavern wall are at about 40% of the maximum peak strength in

seasonal cycling but increase to about 50% in daily cycling. If stresses that exceed 90 % of the maximum peak strength are considered as critical, there should be no such critical zone around the deep cavern.

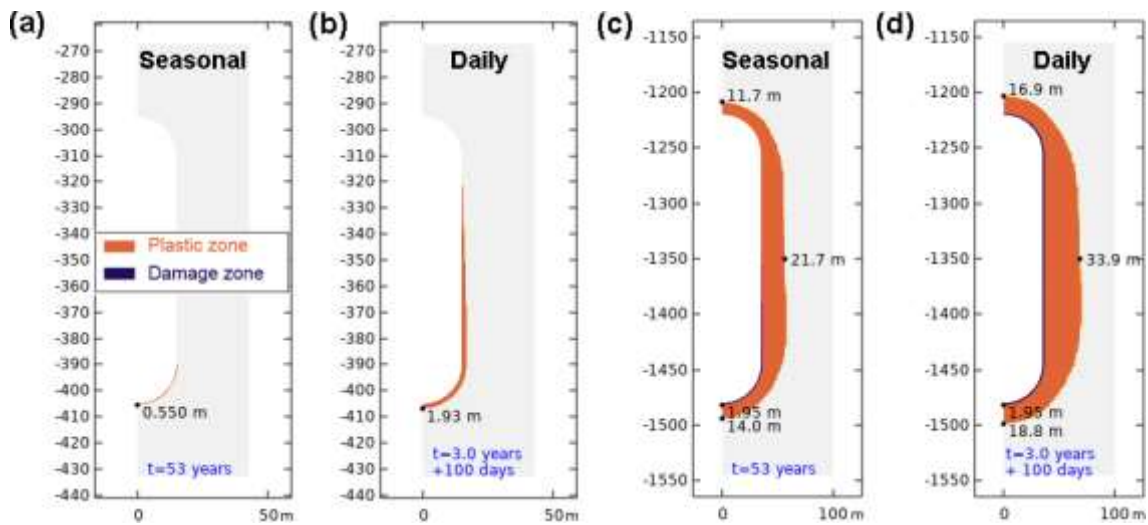


Figure 11.- Plastic and instantaneous damage zones around shallow cavern: (a) seasonal and (b) daily; Deep cavern: (c) seasonal and (d) daily.

In terms of cavern wall displacements, they are in the order of millimetres for the shallow cavern, for both daily and seasonal cycling (Figure 12a). Similar millimetric displacements also occur in the deep cavern in daily cycling (Figure 12b), as only 100 days were analysed. In contrast, in seasonal cycling, the displacements rise to the order of meters after 50 years. A closer look reveals that the cavern sidewall has a maximum horizontal displacement of 3.6 m (Figure 12c) and the cavern floor has a vertical displacement of 3.4 m (Figure 12d). To better observe these displacements in Figure 12a and Figure 12b, in the shallow cavern the horizontal and vertical displacements have been scaled up by a factor of 100, while in the deep cavern they have been scaled up by a factor of 2.5. A quick calculation indicates a cavern volume loss V_L (i.e., reduction) of approximately 17.7% after 50 years for the deep storage (Figure 13a). This represents an estimated loss of 0.34 % per year of activity. The V_L before cycling loading operation (at $t=3$ years) is 0.7%. In the case of daily cycling, results indicate a V_L of 0.0024% per day of activity (i.e., 0.88% per year or 44% after 50 years of activity) still for the deep cavern (Figure 13b). For comparison purpose, when considering a constant gas pressure equal to the maximum gas pressure value (Figure 13c), a similar analysis for the deep cavern gives a V_L of approximately 1.8% at 53 years (i.e. 0.022% volume loss per year of activity). Cavern volume loss is one of the key parameters for assessing the availability of gas storage in underground salt caverns. However, there is no specific design criterion for this parameter. In the literature, Brouard and Berest (1999) and Plaat (2009) suggested that a volume loss of 1% per year is considered acceptable for deep caverns. Wang et al. (2016) and Liu *et al.* (2018) proposed

that the volume loss rate should be lower than 1% in one year, 5% in the first five years, and 30% for the whole design lifetime (usually 30 years). Some natural gas storage salt caverns have experienced large volume losses in a relatively short time. As detailed in Bérest and Brouard (2003), caverns at depths of between 1300 to 2000m have lost up to 40% of their volume. This is due to internal operating pressures and the higher overburden pressure.

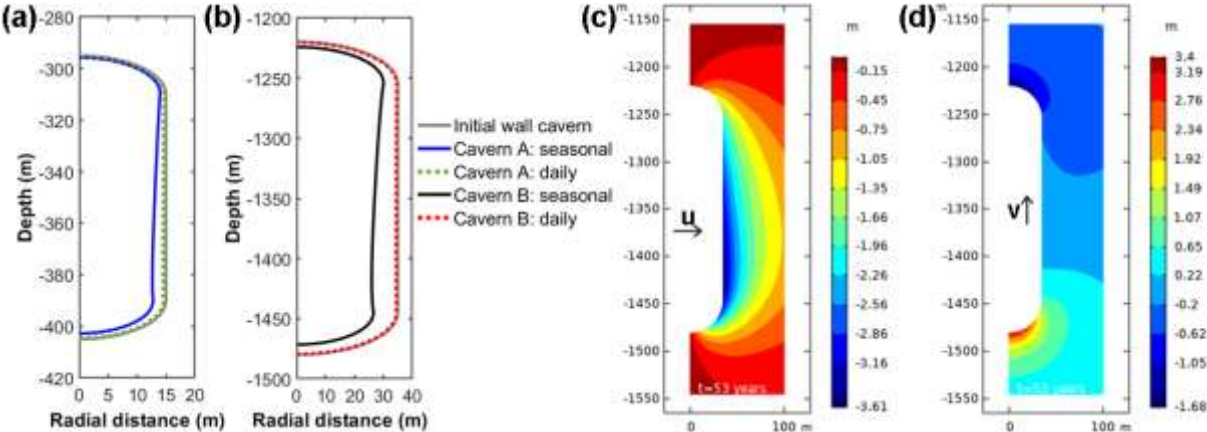


Figure 12.- Total displacements of (a) shallow (x100) and (b) deep (x2.5) cavern walls. (c) Horizontal and (d) vertical displacements of the deep cavern in seasonal cycling.

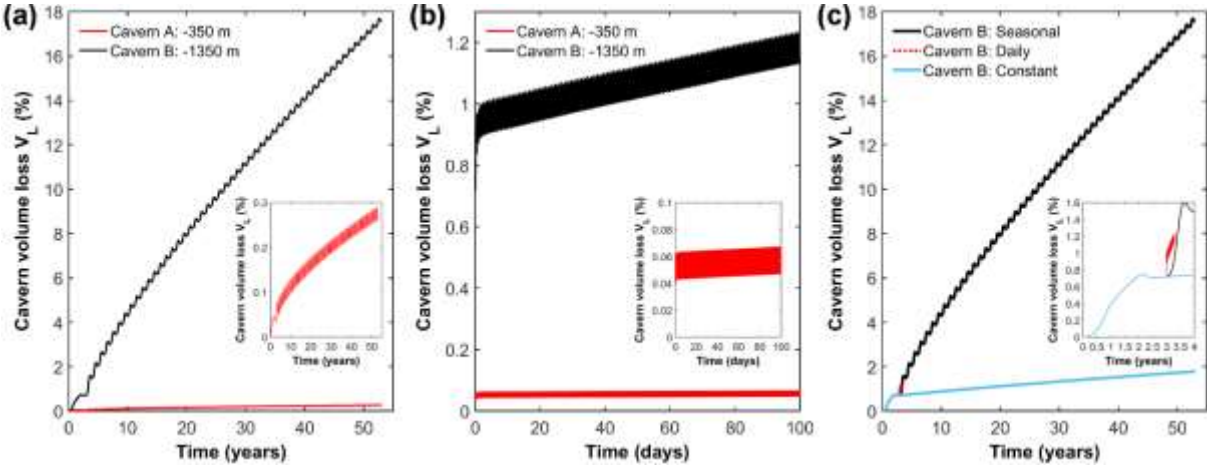


Figure 13.- Cavern volume loss versus time curves for: (a) seasonal and (b) daily cycling; (c) Cavern volume loss versus time curves of deep cavern in seasonal, daily cycling and constant gas pressure, p_g^{max} .

3.3.2. Hydraulic and hydrogen concentration responses

The pore pressure in the horizontal direction from the cavern wall is monitored at specific times during gas operation, as shown in Figure 14. Just before the operating cycle (at $t = 3$ years), the initial pore pressure (respectively, 5.3 MPa in the shallow cavern and 13.3 MPa in the deep cavern) undergoes changes up to a distance of approximately 40 m from the cavern wall in both caverns. During the operating cycle, the decrease in cavern gas pressure in the

withdrawal phase, and therefore of the pore pressure at the wall, induces pore overpressure within the host rock. This overpressure is attributed to the low dissipation rate of excess pore-water pressure that had accumulated previously due to the very low permeability of the rock salt. In the case of seasonal cycling, the pore-water pressure profiles at certain times, such as $t=3.5$ years, 4.5 years, 9.5 years, 52.5 years (Figure 14a and c), highlight the above-mentioned minimum pore-water pressure and pore-water overpressure. The maximum overpressure value is reached at 3.5 years and located at 10 m from the cavern wall. For the shallow cavern, the maximum pore overpressure can reach 0.37 MPa (Figure 14a) against 1.8 MPa for the deep cavern (Figure 14c). In both configurations, the pore-water overpressure gradually dissipates with time and repeated cycling, as shown at the following considered times. At 52.5 years, our numerical simulations forecast a residual pore-water overpressure of 0.07 MPa around the shallow cavern (Figure 14a) and 0.2 MPa around the deep cavern (Figure 14c), respectively. In the case of daily cycling, the pore pressure profiles at specific times, such as $t=3$ years and 4 hours, $t=3$ years, 20 days and 4 hours and $t=3$ years, 80 days and 4 hours (Figure 14b and d), show the minimum and maximum pore-water pressures around both caverns. At 3 years and 4 hours, the pore pressure profile exhibits a nearly vertical drop close the cavern wall (Figure 14b and d). This can be attributed to two factors: the very short time duration between the maximum gas pressure and the minimum gas pressure, and the low permeability of rock salt, which drive pore-pressure dissipation rate within the surrounding rock mass. As time progresses, the repeated withdrawal phases facilitate the overpressure dissipation as observed in the seasonal cycling case. At approximately 3 years and 100 days, the predicted pore-water overpressure around the shallow cavern is 0.42 MPa (Figure 14b), while for the deep cavern (Figure 14d), it is 2.1 MPa. These pore overpressure values are located approximately 7 to 8 meters from the cavern walls.

The pore pressure distributions at the end of the operating cycle are shown in Figure 15. As mentioned above, in seasonal cycling (Figure 15a and c), the pore pressure field is modified within approximately 40 metres from the cavern wall. In a daily scenario (Figure 15b and d) the changes in pore pressure occur close to the cavern wall for both caverns. As predicted in Figure 11, the extent of the damage zone around the caverns is zero (shallow caverns) or very small (deep caverns). This small damage zone observed in the deep cavern (Figure 16a and b) thus induces a modification, but very localized, of permeability in the host rock. The highest permeability changes occur near the floor and the roof of the cavern which is consistent with the findings of Khaledi et al. (2016) and Kumar et al. (2021). However, in terms of permeability, the impact is not significant (Figure 16c and d) with a narrow disturbed permeability zone surrounding the deep cavern.

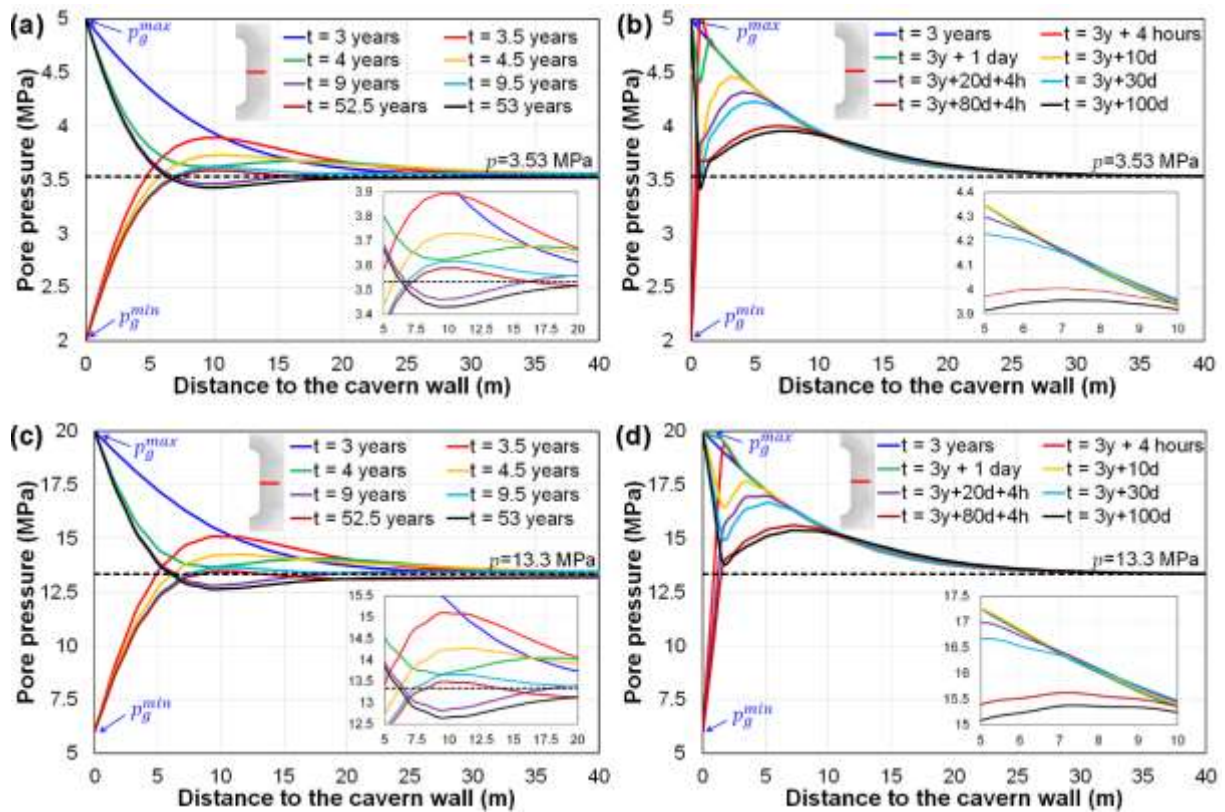


Figure 14.- Pore pressure profiles in the horizontal direction (red line) of shallow cavern: (a) seasonal and (b) daily cycling; Deep cavern: (c) seasonal and (d) daily cycling.

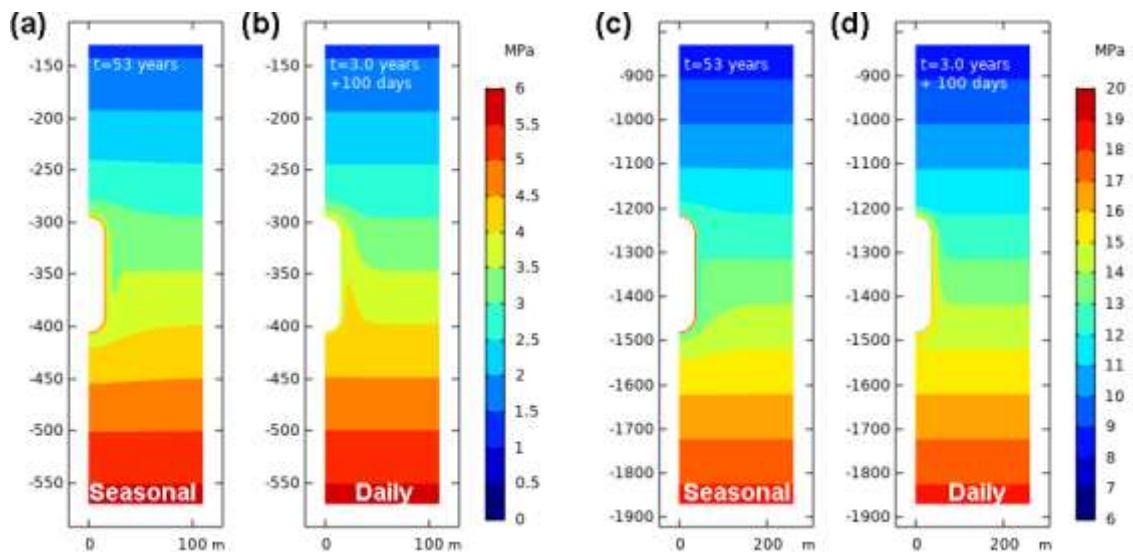


Figure 15.- Pore pressure distribution around shallow cavern: (a) seasonal and (b) daily cycling; Deep cavern: (c) seasonal and (d) daily cycling.

Regarding the hydrogen plume (Figure 17), a similar extension is found for both caverns. It reaches almost 2.5 m in daily cycling and 15 m in seasonal cycling at the end of the operating cycle. An analysis of the modes of hydrogen transport is illustrated in Figure 18, where the ratio of diffusion flux to total flow is calculated. It reveals that more than 40% of the flow at the

cavern wall occurs by diffusion for the deep cavern and this ratio may reach 80% for the shallow cavern. Thus, the hydrogen propagation is done mainly by diffusion, and advection effect is significant only in the near-field vicinity of the cavern walls where the rock salt permeability is modified. This explains why the hydrogen plume extent around the shallow and the deep cavern are globally the same. Fang et al. (2022) also predict a small gas extension around a cavern at 665 m depth and after 30 years of operation.

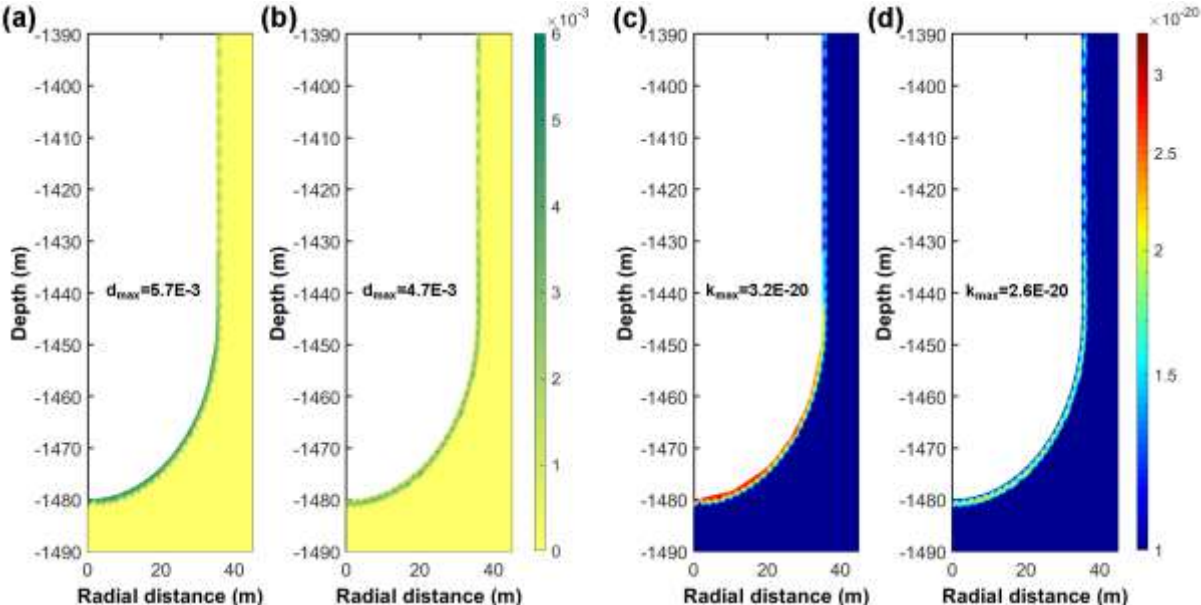


Figure 16.- Instantaneous damage distribution around deep cavern for (a) seasonal and (b) daily cycling. Permeability distribution around deep cavern for (c) seasonal and (d) daily cycling.

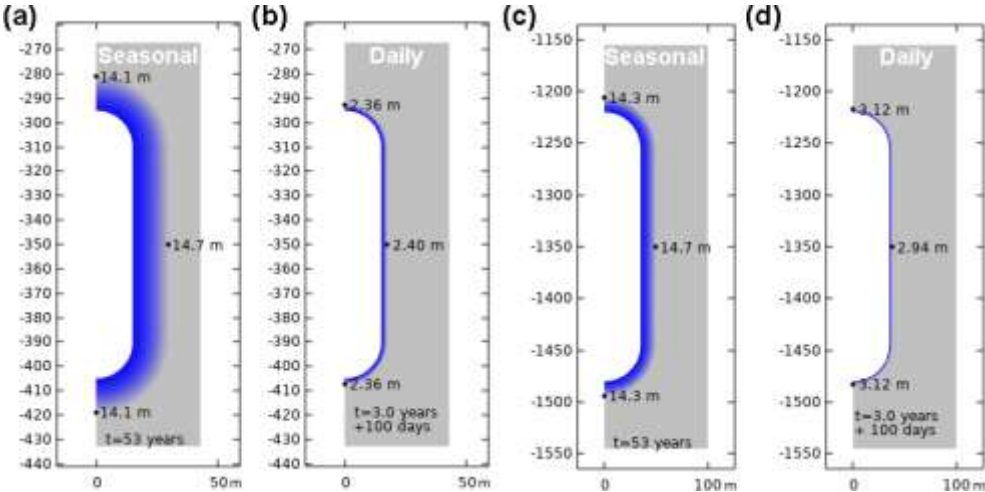


Figure 17.- Hydrogen extension around shallow cavern: (a) seasonal and (b) daily cycling; Deep cavern: (c) seasonal and (d) daily cycling.

As it can be seen, only the mechanical stability of the deep cavern can be compromised in the scenarios analysed. For the hydraulic disturbance and the hydrogen plume length, the same responses are found in both caverns since diffusion mechanism prevails in our simulations. However, with increasing damage, permeability is expected also to increase and possibly

affect more the leakage rate and the plume extent of hydrogen. In order to investigate further the effects of certain material properties or operating conditions, notably rock salt cohesion, gas pressure, initial rock permeability and the damage parameters on the hydrogen leakage, a sensitivity analysis has been carried out (see complementary analysis in Appendix). In this complementary investigation we have focused on the deep cavern subjected to seasonal cycling, which represents the most critical case with regard to the storage integrity and offers more interesting hydromechanical results.

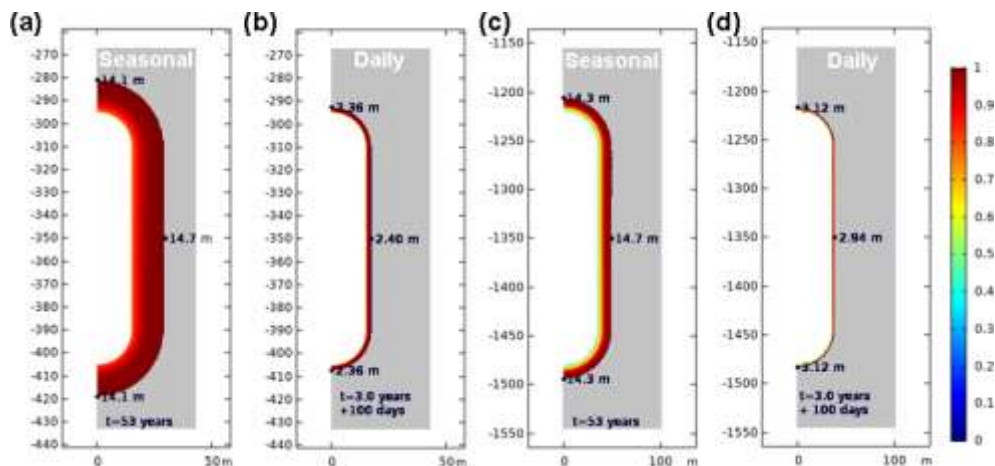


Figure 18.- Diffusion flux/ Total flow of shallow cavern: (a) seasonal and (b) daily cycling; Deep cavern: (c) seasonal and (d) daily cycling.

Main results of this sensitivity analysis indicate that: (i) the extension of the plastic zone is influenced by the decrease in cohesion and the minimum internal operating pressure; (ii) the extension of instantaneous damage zone modifies the transport properties significantly when the damage threshold is modified; (iii) high cavern wall deformations and cavern volume loss are determined for very low minimum operating pressures; (iv) the tertiary creep increases as the resistance parameters and/or the minimum gas pressure value decrease; and (v) there is a small increase in hydrogen extension resulting from the modification of the permeability around the cavern wall.

4. Conclusions and perspectives

In this study, we examine the feasibility and assess the risks of using salt caverns for underground hydrogen storage. Based on the mechanical and hydraulic properties of rock salt observed from experimental data, as well as on some available rheological models related to this material, we propose a model that allows considering the short-term and long-term behaviours of rock salt. The short-term model takes into account elastoplastic and instantaneous damage behaviours. This model is based on the Mohr-Coulomb criterion and its main features include: a plastic hardening phase; volumetric dilatancy which disappears by

increasing confining pressures and an instantaneous damage variable that initiates from the dilatancy criterion. For the long-term behaviour, the three creep phases generally observed on creep tests are considered: transient creep, steady-state creep, and tertiary creep. These are respectively based on the Kelvin model, Norton law, and the continuum damage mechanics theory. Thus, this model describes some of the main key mechanisms of rock salt behaviour. The resulting model is applied to investigate the hydromechanical behaviour of vertical salt caverns, for shallow (-350 m) and very deep (-1350 m) underground hydrogen storage, with a focus on the impact of seasonal and daily operation cycles. The results indicate that the deep cavern is more susceptible to mechanical stability problems. The daily scenario is also more detrimental to the stability. However, considering the hydrogen extension, the amount of gas leakage is limited and both caverns lead to almost the same plume size because of diffusion which is preponderant. Even if up to 6 orders of magnitude change in permeability can be achieved as a function of the damage threshold considered, the increase in hydrogen plume extension still remains very small. Under the assumptions made, these findings suggest that the use of salt caverns for green hydrogen storage, even with aggressive operating conditions to regulate variations between renewable energy production and peak power demands, should not significantly affect the stability of salt cavern nor promote an increase in hydrogen loss.

Perspectives of the model would be to consider dynamic mechanical fatigue and the influence of temperature on the mechanical behaviour of rock salt. Further investigations are required to assess their impact on hydrogen plume extension.

Declaration of Competing Interest

We declare that we have no financial and personal relationships with other people or organizations that can inappropriately influence our work, there is no professional or other personal interest of any nature or kind in any product, service, or company that could be construed as influencing, the position presented in the manuscript.

Acknowledgements

This research was funded by the French Scientific Interest Group GEODENERGIES in the framework of the ROSTOCK-H project (Risks and Opportunities of the Geological Storage of Hydrogen in Salt Caverns in France and Europe) and by the Grand Est Regional Council.

Appendix A. Supplementary material

Supplementary material associated with this article can be found in the online version at <https://doi.org/10.1016/j.compgeo.2023.105690>

References

- Alkan H, Cinar Y, Pusch G (2007) Rock salt dilatancy boundary from combined acoustic emission and triaxial compression tests. *Int J Rock Mech Min Sci* 44:108–119. <https://doi.org/10.1016/j.ijrmms.2006.05.003>
- Asgari A, Ramezanzadeh A, Jalali SME, Brouard B (2020) Stability Analysis of Salt Cavern Gas Storage Using 2D Thermo-Hydro-Mechanical Finite-Element Software. *J Min Environ* 11:.. <https://doi.org/10.22044/jme.2019.8357.1715>
- Aubertin M, Julien MR, Servant S, Gill DE (1999) A rate-dependent model for the ductile behavior of salt rocks. *Can Geotech J* 36:660–674. <https://doi.org/10.1139/t99-033>
- Bérest P (2019) Heat transfer in salt caverns. *Int J Rock Mech Min Sci* 120:82–95. <https://doi.org/10.1016/j.ijrmms.2019.06.009>
- Bérest P (2013) The Mechanical Behavior of Salt and Salt Caverns. In: Marek Kwasniewski M, Lydzba D (eds) *Proceedings of Eurock 2013*. CRC Press, London, pp 17–30
- Bérest P, Brouard B (2003) Safety of Salt Caverns Used for Underground Storage Blow Out; Mechanical Instability; Seepage; Cavern Abandonment. *Oil Gas Sci Technol* 58:361–384. <https://doi.org/10.2516/ogst:2003023>
- Bérest P, Karimi-Jafari M, Brouard B, Bazargan B (2006) In situ mechanical tests in salt caverns. In: *Proc. Technical Class, SMRI Spring Meeting*. Brussels, pp 91–130
- Brouard B, Berest P (1998) A tentative classification of salts according to their creep properties. In: *SMRI spring 1998 meeting*. New Orleans, pp 1–21
- Brouard B, Bérest P, Djizanne H, Frangi A (eds) (2012) Mechanical stability of a salt cavern submitted to high-frequency cycles. In: *Mechanical Behaviour of Salt VII*. CRC Press, pp 381–389
- Caglayan DG, Weber N, Heinrichs HU, et al (2020) Technical potential of salt caverns for hydrogen storage in Europe. *Int J Hydrog Energy* 45:6793–6805. <https://doi.org/10.1016/j.ijhydene.2019.12.161>
- Chen J, Ren S, Yang C, et al (2013) Self-Healing Characteristics of Damaged Rock Salt under Different Healing Conditions. *Materials* 6:3438–3450. <https://doi.org/10.3390/ma6083438>
- Chiarelli AS, Shao JF, Hoteit N (2003) Modeling of elastoplastic damage behavior of a claystone. *Int J Plast* 19:23–45. [https://doi.org/10.1016/S0749-6419\(01\)00017-1](https://doi.org/10.1016/S0749-6419(01)00017-1)
- Cosenza P, Ghoreychi M (1999) Effects of very low permeability on the long-term evolution of a storage cavern in rock salt. *Int J Rock Mech Min Sci* 36:527–533. [https://doi.org/10.1016/S0148-9062\(99\)00018-2](https://doi.org/10.1016/S0148-9062(99)00018-2)
- Cristescu ND (1993) A general constitutive equation for transient and stationary creep of rock salt. *Int J Rock Mech Min Sci Geomech Abstr* 30:125–140. [https://doi.org/10.1016/0148-9062\(93\)90705-1](https://doi.org/10.1016/0148-9062(93)90705-1)
- DeVries KL, Mellegard KD, Callahan GD, Goodman WM (2005) Cavern roof stability for natural gas storage in bedded salt. United States Department of Energy National Energy Technology Laboratory Topical Report RSI-1829, DE-FG26-02NT41651, Pittsburgh
- Djizanne H, Bérest P, Brouard B, Frangi A (2014) Blowout in Gas Storage Caverns. *Oil Gas Sci Technol – Rev D'IFP Energ Nouv* 69:1251–1267. <https://doi.org/10.2516/ogst/2013208>
- Fang Y, Hou Z, Yue Y, et al (2022) Numerical study of hydrogen storage cavern in thin-bedded rock salt, Anning of China. In: *The Mechanical Behavior of Salt X*, 1st edn. CRC Press, London, pp 652–661
- Fossum AF, Brodsky NS, Chan KS, Munson DE (1993) Experimental evaluation of a constitutive model for inelastic flow and damage evolution in solids subjected to triaxial compression. *Int J Rock Mech Min Sci Geomech Abstr* 30:1341–1344. [https://doi.org/10.1016/0148-9062\(93\)90119-X](https://doi.org/10.1016/0148-9062(93)90119-X)
- Fuenkajorn K, Phueakphum D (2010) Effects of cyclic loading on mechanical properties of Maha Sarakham salt. *Eng Geol* 112:43–52. <https://doi.org/10.1016/j.enggeo.2010.01.002>

- Gawin D, Pesavento F, Schrefler BA (2002) Simulation of damage-permeability coupling in hygro-thermo-mechanical analysis of concrete at high temperature. *Commun Numer Methods Eng* 18:113–119. <https://doi.org/10.1002/cnm.472>
- Grgic D (2016) Constitutive modelling of the elastic–plastic, viscoplastic and damage behaviour of hard porous rocks within the unified theory of inelastic flow. *Acta Geotech* 11:95–126. <https://doi.org/10.1007/s11440-014-0356-6>
- Grgic D, Al Sahyouni F, Golfier F, et al (2022) Evolution of Gas Permeability of Rock Salt Under Different Loading Conditions and Implications on the Underground Hydrogen Storage in Salt Caverns. *Rock Mech Rock Eng* 55:691–714. <https://doi.org/10.1007/s00603-021-02681-y>
- Guo Y, Yang C, Mao H (2012) Mechanical properties of Jintan mine rock salt under complex stress paths. *Int J Rock Mech Min Sci* 56:54–61. <https://doi.org/10.1016/j.ijrmms.2012.07.025>
- Habibi R, Moomivand H, Ahmadi M, Asgari A (2021) Stability analysis of complex behavior of salt cavern subjected to cyclic loading by laboratory measurement and numerical modeling using LOCAS (case study: Nasrabad gas storage salt cavern). *Environ Earth Sci* 80:317. <https://doi.org/10.1007/s12665-021-09620-8>
- Heusermann S, Rolfs O, Schmidt U (2003) Nonlinear finite-element analysis of solution mined storage caverns in rock salt using the LUBBY2 constitutive model. *Comput Struct* 81:629–638. [https://doi.org/10.1016/S0045-7949\(02\)00415-7](https://doi.org/10.1016/S0045-7949(02)00415-7)
- Hou Z (2003) Mechanical and hydraulic behavior of rock salt in the excavation disturbed zone around underground facilities. *Int J Rock Mech Min Sci* 40:725–738. [https://doi.org/10.1016/S1365-1609\(03\)00064-9](https://doi.org/10.1016/S1365-1609(03)00064-9)
- Hunsche U, Hampel A (1999) Rock salt — the mechanical properties of the host rock material for a radioactive waste repository. *Eng Geol* 52:271–291. [https://doi.org/10.1016/S0013-7952\(99\)00011-3](https://doi.org/10.1016/S0013-7952(99)00011-3)
- Ineris (2022) State of knowledge on the storage of hydrogen in salt caverns. Verneuil-en-Halatte : Ineris-206731-v1.0
- Khaledi K, Mahmoudi E, Datcheva M, Schanz T (2016) Stability and serviceability of underground energy storage caverns in rock salt subjected to mechanical cyclic loading. *Int J Rock Mech Min Sci* 86:115–131. <https://doi.org/10.1016/j.ijrmms.2016.04.010>
- Kumar KR, Makhmutov AA, Spiers CJ, Hajibeygi H (2021) Geomechanical simulation of energy storage in salt formations. *Sci Rep* 11:19640. <https://doi.org/10.1038/s41598-021-99161-8>
- Li W, Miao X, Yang C (2020) Failure analysis for gas storage salt cavern by thermo-mechanical modelling considering rock salt creep. *J Energy Storage* 32:102004. <https://doi.org/10.1016/j.est.2020.102004>
- Liang W, Yang C, Zhao Y, et al (2007) Experimental investigation of mechanical properties of bedded salt rock. *Int J Rock Mech Min Sci* 44:400–411. <https://doi.org/10.1016/j.ijrmms.2006.09.007>
- Liang WG, Zhao YS, Xu SG, Dusseault MB (2011) Effect of strain rate on the mechanical properties of salt rock. *Int J Rock Mech Min Sci* 48:161–167. <https://doi.org/10.1016/j.ijrmms.2010.06.012>
- Liu J, Xie H, Hou Z, et al (2014) Damage evolution of rock salt under cyclic loading in uniaxial tests. *Acta Geotech* 9:153–160. <https://doi.org/10.1007/s11440-013-0236-5>
- Liu W, Jiang D, Chen J, et al (2018) Comprehensive feasibility study of two-well-horizontal caverns for natural gas storage in thinly-bedded salt rocks in China. *Energy* 143:1006–1019. <https://doi.org/10.1016/j.energy.2017.10.126>
- Liu W, Zhang X, Li H, Chen J (2020) Investigation on the Deformation and Strength Characteristics of Rock Salt Under Different Confining Pressures. *Geotech Geol Eng* 38:5703–5717. <https://doi.org/10.1007/s10706-020-01388-1>
- Ma H, Yang C, Li Y, et al (2015) Stability evaluation of the underground gas storage in rock salts based on new partitions of the surrounding rock. *Environ Earth Sci* 73:6911–6925. <https://doi.org/10.1007/s12665-015-4019-1>

- Mazars J (1984) Application of Continuous Damage Mechanic to Non-Linear Behavior of Concrete Structures. Ph.D. Thesis, Paris 6 University
- Munson DE, Dawson PR (1979) Constitutive model for the low temperature creep of salt (with application to WIPP)
- Ozarslan A (2012) Large-scale hydrogen energy storage in salt caverns. *Int J Hydrog Energy* 37:14265–14277. <https://doi.org/10.1016/j.ijhydene.2012.07.111>
- Peach CJ (1991) Influence of deformation on the fluid transport properties of salt rocks. Ph.D. Thesis, Facultiet Aardwetenschappen der Rijksuniversiteit Utrecht
- Peach CJ, Spiers CJ (1996) Influence of crystal plastic deformation on dilatancy and permeability development in synthetic salt rock. *Tectonophysics* 256:101–128. [https://doi.org/10.1016/0040-1951\(95\)00170-0](https://doi.org/10.1016/0040-1951(95)00170-0)
- Plaat H (2009) Underground gas storage: Why and how. *Geol Soc Lond Spec Publ* 313:25–37. <https://doi.org/10.1144/SP313.4>
- Popp T, Kern H, Schulze O (2001) Evolution of dilatancy and permeability in rock salt during hydrostatic compaction and triaxial deformation. *J Geophys Res Solid Earth* 106:4061–4078. <https://doi.org/10.1029/2000JB900381>
- Popp T, Wiedemann M, Kansy A, Pusch G (2007) Gas transport in dry rock salt – implications from laboratory investigations and field studies. In: Wallner M, Lux K-H, Minkley W, Hardy HR (eds) *The Mechanical Behavior of Salt – Understanding of THMC Processes in Salt*, 1st edn. CRC Press, pp 17–26
- Reedlunn B, Argüello JG, Hansen FD (2022) A reinvestigation into Munson’s model for room closure in bedded rock salt. *Int J Rock Mech Min Sci* 151:105007. <https://doi.org/10.1016/j.ijrmms.2021.105007>
- Salzer K, Günther R, Minkley W, et al (2015) Joint project III on the comparison of constitutive models for the mechanical behavior of rock salt II: Extensive laboratory test program with clean salt from WIPP. In: Roberts L (ed) *Mechanical Behaviour of Salt VIII*. CRC Press, pp 3–12
- Schulze O, Popp T, Kern H (2001) Development of damage and permeability in deforming rock salt. *Eng Geol* 61:163–180. [https://doi.org/10.1016/S0013-7952\(01\)00051-5](https://doi.org/10.1016/S0013-7952(01)00051-5)
- Senseny PE, Hansen FD, Russell JE, et al (1992) Mechanical behaviour of rock salt: Phenomenology and micromechanisms. *Int J Rock Mech Min Sci Geomech Abstr* 29:363–378. [https://doi.org/10.1016/0148-9062\(92\)90513-Y](https://doi.org/10.1016/0148-9062(92)90513-Y)
- Shahmorad Z, Salarirad H, Molladavoudi H (2016) A study on the effect of utilizing different constitutive models in the stability analysis of an underground gas storage within a salt structure. *J Nat Gas Sci Eng* 33:808–820. <https://doi.org/10.1016/j.jngse.2016.06.011>
- Souley M, Vu M-N, Armand G (2022) 3D Modelling of Excavation-Induced Anisotropic Responses of Deep Drifts at the Meuse/Haute-Marne URL. *Rock Mech Rock Eng* 55:4183–4207. <https://doi.org/10.1007/s00603-022-02841-8>
- Stormont JC (1997) In situ gas permeability measurements to delineate damage in rock salt. *Int J Rock Mech Min Sci* 34:1055–1064. [https://doi.org/10.1016/S1365-1609\(97\)90199-4](https://doi.org/10.1016/S1365-1609(97)90199-4)
- Stormont JC, Daemen JJK, Desai CS (1992) Prediction of dilation and permeability changes in rock salt. *Int J Numer Anal Methods Geomech* 16:545–569. <https://doi.org/10.1002/nag.1610160802>
- Thorel L (1994) Plasticité et endommagement des roches ductiles. Application au sel gemme. Ph.D. Thesis, École National des Ponts et Chaussées
- Wang G, Guo K, Christianson M, Konietzky H (2011) Deformation characteristics of rock salt with mudstone interbeds surrounding gas and oil storage cavern. *Int J Rock Mech Min Sci* 48:871–877. <https://doi.org/10.1016/j.ijrmms.2011.06.012>
- Wang T, Yan X, Yang H, et al (2013) A new shape design method of salt cavern used as underground gas storage. *Appl Energy* 104:50–61. <https://doi.org/10.1016/j.apenergy.2012.11.037>
- Wang T, Yang C, Ma H, et al (2016) Safety evaluation of salt cavern gas storage close to an old cavern. *Int J Rock Mech Min Sci* 83:95–106. <https://doi.org/10.1016/j.ijrmms.2016.01.005>

- Wawersik WR, Hannum DW (1980) Mechanical behavior of New Mexico rock salt in triaxial compression up to 200°C. *J Geophys Res* 85:891. <https://doi.org/10.1029/JB085iB02p00891>
- Wu F, Chen J, Zou Q (2019) A nonlinear creep damage model for salt rock. *Int J Damage Mech* 28:758–771. <https://doi.org/10.1177/1056789518792649>
- Yang C, Daemen JJK, Yin J-H (1999) Experimental investigation of creep behavior of salt rock. *Int J Rock Mech Min Sci* 36:233–242. [https://doi.org/10.1016/S0148-9062\(98\)00187-9](https://doi.org/10.1016/S0148-9062(98)00187-9)
- Zhang D, Skoczylas F, Agostini F, Jeannin L (2020) Experimental Investigation of Gas Transfer Properties and Stress Coupling Effects of Salt Rocks. *Rock Mech Rock Eng* 53:4015–4029. <https://doi.org/10.1007/s00603-020-02151-x>
- Zhou H, Hu D, Zhang F, Shao J (2011) A thermo-plastic/viscoplastic damage model for geomaterials. *Acta Mech Solida Sin* 24:195–208. [https://doi.org/10.1016/S0894-9166\(11\)60021-9](https://doi.org/10.1016/S0894-9166(11)60021-9)
- Zivar D, Kumar S, Foroozesh J (2021) Underground hydrogen storage: A comprehensive review. *Int J Hydrog Energy* 46:23436–23462. <https://doi.org/10.1016/j.ijhydene.2020.08.138>